

# High Latitude Ionospheric Electrodynamics During STEVE and non-STEVE Substorm Events

V. Svaldi<sup>1</sup>, T. Matsuo<sup>2</sup>, L. Kilcommons<sup>2</sup>, and B. Gallardo-Lacourt<sup>3,4</sup>

<sup>1</sup>Mechanical Engineering Department, Colorado School of Mines, Golden, CO, USA

<sup>2</sup>Ann & H.J Smead Department of Aerospace Engineering Sciences, University of Colorado, Boulder, CO,  
USA

<sup>3</sup>Goddard Space Flight Center, National Aeronautics and Space Administration, Greenbelt, MD, USA

<sup>4</sup>Universities of Space Research Association, Columbia, MD, USA

## Key Points:

- First STEVE study focused on global convection patterns shows a strong dawn-cell extending into subauroral pre-midnight sector
- First application of AMGeO to magnetosphere-ionosphere coupling research, involving 32 STEVE and 32 non-STEVE substorms
- Larger cross-polar cap potential drop and more prolonged nightside asymmetry found in STEVE ionospheric convection patterns

16 **Abstract**

17 Previous studies have shown that Strong Thermal Emission Velocity Enhancement (STEVE)  
18 events occur at the end of a prolonged substorm expansion phase. However, the connection  
19 between STEVE occurrence and substorms and the global high-latitude ionospheric elec-  
20 trodynamics associated with the development of STEVE and non-STEVE substorms are  
21 not yet well understood. The focus of this paper is to identify electrodynamic features  
22 that are unique to STEVE events through a comprehensive analysis of ionospheric convec-  
23 tion patterns estimated from SuperDARN plasma drift and ground-based magnetometer  
24 data using the Assimilative Mapping of Geospace Observations (AMGeO) procedure. Re-  
25 sults from AMGeO are further analyzed using principal component analysis and superposed  
26 epoch analysis for 32 STEVE and 32 non-STEVE substorm events. The analysis shows that  
27 the magnitude of cross-polar cap potential drop is generally greater for STEVE events. In  
28 contrast to non-STEVE substorms, the majority of STEVE events investigated accompany  
29 with a pronounced extension of the dawn cell into the pre-midnight subauroral latitudes,  
30 reminiscent of the Harang reversal convection feature where the eastward electrojet overlaps  
31 with the westward electrojet, which tends to prolong over substorm expansion and recov-  
32 ery phases. This is consistent with the presence of an enhanced subauroral electric field  
33 confirmed by previous STEVE studies. The global and localized features of high-latitude  
34 ionospheric convection associated with optical STEVE events characterized in this paper  
35 provide important insights into cross-scale magnetosphere-ionosphere coupling mechanisms  
36 that differentiate STEVE events from non-STEVE substorm events.

37 **Plain Language Summary**

38 In 2016, citizen observers introduced a mysterious subauroral phenomenon called Strong  
39 Thermal Emission Velocity Enhancement (STEVE) to the scientific community. STEVE  
40 events are characterized by the presence of a thin and bright purple emission located closer  
41 to the horizon than the typical aurora. The focus of this paper is to quantify characteristic  
42 features of the global ionosphere during STEVE events, and to investigate their relationship  
43 to related phenomena known as substorms using a newly developed data science tool named  
44 Assimilative Mapping of Geospace Observation (AMGeO). In this study, using AMGeO, we  
45 analyze large amounts of ground-based data during 32 STEVE events as well as 32 non-  
46 STEVE substorm events. Findings from the study are helpful to understand differences in  
47 the way the magnetosphere is coupled to the ionosphere during STEVE events and non-  
48 STEVE substorms.

## 1 Introduction

In 2016, a Canadian citizen scientist community of auroral photographers introduced a new optical ionospheric phenomenon to the scientific community. Initially referred to as proton arc by the citizen scientists, the optical structure has been named STEVE, a term initially chosen for its lack of scientific implications (Gallardo-Lacourt et al., 2019). To better reflect STEVE's observed physical characteristics, the name was later converted into the backronym, standing for *Strong Thermal Emission Velocity Enhancement*. STEVE is typically observed as a dynamic, thin, westward aligned structure that has bright purple and white emission at subauroral latitudes, equatorward of the auroral oval. STEVE is sometimes accompanied by distinct green finger-like structures known as the "picket fence". Additionally, STEVE is known to be connected to intense subauroral ion drifts (SAIDs) (Archer et al., 2019a; MacDonald et al., 2018). STEVE's emission mechanism has been determined to be different from traditional aurora which are usually associated with energetic electron and ion precipitation (GallardoLacourt et al., 2018; Nishimura et al., 2019). Gillies et al. (2019) have used the newly deployed Transition Region Explorer (TREx) Spectrograph to study STEVE's peculiar mauve emission, and found that STEVE's spectrum corresponds to a continuous emission over 400-800 nm wavelengths. The altitude of STEVE's emission calculated using image triangulation suggests that STEVE occurs between 130-270 km (Archer et al., 2019b; Liang et al., 2019). Taking all these properties into consideration, Harding et al. (2020) have formulated a formation mechanism for STEVE's continuum emission that is distinct from commonly known auroral emission mechanisms. Thanks to these past work, some properties of STEVE are relatively well characterized, however the magnetosphere-ionosphere coupling mechanisms driving these STEVE events are still not completely understood.

The connection between STEVE occurrence and substorms is one of the active research topics in magnetosphere-ionosphere coupling. Previous studies have shown that STEVE occurs at the end of a prolonged expansion phase and that substorms without STEVE are more common than substorm events with STEVE (GallardoLacourt et al., 2018). This indicates that there are unique types of substorms that have the favorable conditions for STEVE to occur (GallardoLacourt et al., 2018; Nishimura et al., 2020). In particular, Nishimura et al. (2020) have analyzed the location of the substorm surge and found that the surge and the injection location rapidly shifts duskward for substorm events when STEVE is observed; while for non-STEVE substorms, the injection location stays around midnight. The authors have also reported that simulation results with the Rice Convection Model with an equilibrated magnetic field model show that the shifting of the injection location contributes to the subauroral polarization streams (SAPS) electric fields becoming narrower and more intense. These results reported in previous studies suggest that although STEVE is not produced by magnetospheric particles precipitating into the Earth's upper atmosphere, the magnetosphere plays a critical role by creating the likely conditions for STEVE to form in the ionosphere.

In this study we analyze the global high-latitude ionospheric response during substorm events with and without STEVE. We utilize the Assimilative Mapping of Geospace Observations (AMGeO) (Matsuo, 2020), available as a newly developed open source data science research tool (AMGeO Collaboration, 2019), to combine ground-based plasma drifts from the Super Dual Auroral Radar Network (SuperDARN) (Chisham et al., 2007) and ground-based magnetic fields from worldwide magnetometers (Gjerloev, 2012). The DMSP SSJ electron precipitation data (Redmon et al., 2017) are also used to determine the conductance. A total of 64 events over the years of 2008-2018, including 32 STEVE events from the study by (GallardoLacourt et al., 2018) and 32 non-STEVE substorm events identified in SuperMAG data base (Newell & Gjerloev, 2011), are investigated using the AMGeO procedure. As an example of AMGeO's capabilities, Figure 1 shows the global ionospheric convection pattern estimated using AMGeO from SuperDARN line-of-sight plasma drift and SuperMAG ground-based magnetometer data along with in-situ measurements of electron

102 temperature, density and crosstrack ion velocity from the coincident SWARM satellite pass  
 103 during STEVE occurring on July 25, 2016. Swarm measurements for this event are previ-  
 104 ously presented in MacDonald et al. (2018). Elevated electron temperature, electron density  
 105 depletion, and well-defined narrow fast westward plasma flow at peak of optical emission  
 106 are key signatures of STEVE (Archer et al., 2019a; MacDonald et al., 2018). These key  
 107 signatures are also present in 8 of the 32 STEVE events investigated in the study by (Archer  
 108 et al., 2019a). Note that localized westward plasma flows associated with STEVE, reaching  
 109 as fast as 5.5 km/s, cannot be resolved by AMGeO and that typical plasma drift speed asso-  
 110 ciated with the usual two-cell convection is on the order of 500-1000 m/s. Instead of highly  
 111 localized plasma flows, this study focuses on global high-latitude ionospheric electrody-  
 112 namics, so the convection patterns estimated by AMGeO for 64 events are further analyzed using  
 113 principal component analysis (PCA) to characterize global modes of convection variability  
 114 associated with STEVE and non-STEVE substorm events. A superposed epoch analysis  
 115 approach is also used to determine correlations of the time-varying magnitude of princi-  
 116 pal components (PC) to solar wind parameters and geomagnetic activity indices for both  
 117 categories of events.

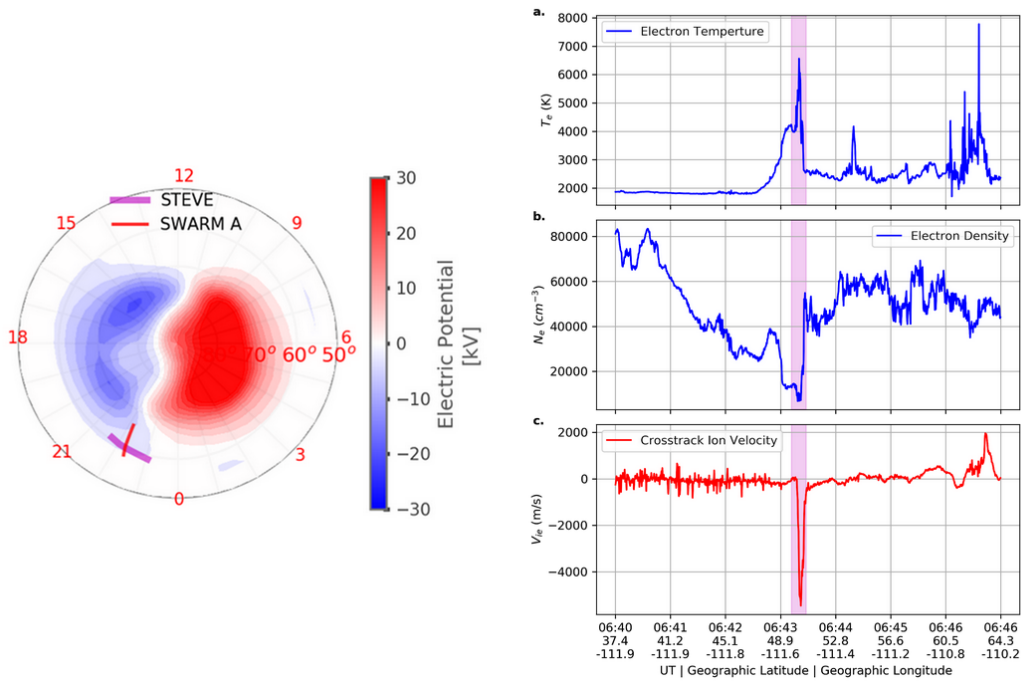


**Figure 1.** (Left) Global ionospheric convection pattern estimated by AMGeO, with overlays of STEVE locations as reported by ground-based instruments and observers in the pre-midnight sector (magenta), and Swarm A satellite track (red). (Right) Swarm A satellite in-situ measurements along the pass on July 25, 2016 that coincides with STEVE optical emission: a.) Electron temperature; b.) Electron number density; and c.) Ion velocity (positive value is eastward flow).

118 The paper is structured as follows. Following a description of STEVE and non-STEVE  
 119 substorm event selections, data sets and data analysis approaches, including assimilative  
 120 mapping, principal component analysis and superposed epoch analysis, used in this study are  
 121 given in Section 2, results from comparative analysis of STEVE and non-STEVE substorm  
 122 convection patterns estimated by AMGeO are presented in Section 3. Section 4 summarizes  
 123 key differences between STEVE and non-STEVE substorm events identified in Section 3 as  
 124 tables. Discussion and conclusions are given in Sections 5 and 6.

## 2 Data Set and Data Analysis Approach

This section provides details pertaining to the STEVE and non-STEVE substorm events, data, and data analysis approaches used in this study. Section 2.1 discusses the events selected including the specific dates and onset times in UT for all STEVE and non-STEVE substorm events occurring between the years 2008 and 2018. Section 2.2 explains the assimilative mapping procedure and data ingested in order to generate assimilative maps of high-latitude ionospheric convection patterns. Post analysis techniques performed, including principal component analysis, superposed epoch analysis, and reconstruction of electrostatic potential distribution, are described in Section 2.3.

### 2.1 Event Selection over 2008-2018

The 32 STEVE events investigated in this study are identified using the Time History of Events and Macroscale Interactions during Substorms (THEMIS) and the Redline Geospace Observatory (REGO) groundbased AllSky Imagers (ASIs) managed by the University of Calgary (GallardoLacourt et al., 2018). Table 1 shows a list of these events, occurring between the years of 2008 and 2018. 28 of these events are previously investigated by GallardoLacourt et al. (2018) wherein 21 events are identified by THEMIS ASI and 7 by REGO ASI. The 4 additional STEVE events are identified using REGO ASI data. The start time of the STEVE events (as shown in Table 1), hereafter referred to as the STEVE optical onset, is the UT time at which STEVE is first detected in the optical data from the THEMIS and REGO ASIs (GallardoLacourt et al., 2018). In ASI images, STEVE optical features appear as its distinct long, narrow structure located equatorward of the auroral oval. One important aspect to consider is that STEVE optical onset time definition is limited by the camera field-of-view. Since STEVE is a westward moving structure, it is possible that the initial formation of STEVE could occur eastward of the camera field-of-view. This may lead to a potential time difference between STEVE's real onset and what is defined here as STEVE optical onset. Nevertheless, since STEVE propagates rapidly westward this timing ambiguity should not significantly affect our results.

**Table 1.** List of dates and UT onset times of 32 STEVE events identified optically using ASI (GallardoLacourt et al., 2018).

Event	Date	STEVE Onset	Event	Date	STEVE Onset
1	2-11-2008	9:30	17	2-20-2012	8:40
2	3-26-2008	7:20	18	9-13-2013	8:30
3	3-27-2008	3:00	19	8-21-2014	9:20
4	3-28-2008	2:00	20	9-7-2015	5:35
5	3-28-2008	7:22	21	9-11-2015	5:20
6	4-12-2008	8:00	22	2-8-2016	6:30
7	5-4-2008	8:00	23	4-17-2016	5:10
8	7-12-2008	3:40	24	7-25-2016	6:00
9	3-11-2010	6:00	25	7-29-2016	5:20
10	4-4-2010	7:20	26	8-22-2017	3:08
11	4-5-2010	5:30	27	8-24-2017	6:11
12	8-3-2010	5:40	28	9-18-2017	6:35
13	9-17-2010	7:00	29	9-27-2017	6:41
14	4-2-2011	6:47	30	3-25-2018	7:46
15	4-20-2011	8:38	31	4-10-2018	5:10
16	6-23-2011	7:00	32	7-17-2018	6:30

Event dates with top 10 greatest minimum SML values are highlighted in red

152 The 32 non-STEVE substorm events are selected, using the SuperMAG substorm  
 153 database, from the Newell and Gjerloev (2011) substorm list which covers a time range  
 154 from 1969 to the current. Substorms that have occurred in the absence of STEVE are se-  
 155 lected as control events so that non-STEVE substorms have the same relative month, year,  
 156 and onset UT time as the STEVE events as indicated by dates and times for all 64 events  
 157 listed in Tables 1-2). These STEVE and non-STEVE substorm events are both analyzed  
 158 every 5 minutes for a 3 hour duration, including 1.5 hour prior and 1.5 hour post the onset  
 159 time using the same data analysis approach described next.

160 The mean and minimum values of SML, which is the SuperMAG version of the AL-  
 161 index available at a 1-min cadence (Newell & Gjerloev, 2011), are also considered in the  
 162 selection of non-STEVE substorm events. The variability in SML mean, minimum and  
 163 standard deviation for STEVE and non-STEVE substorm events are shown in Figure 2.  
 164 While the average of SML minimum value for STEVE events is -727 nT with a standard  
 165 deviation of 220 nT, it is -605 nT with a standard deviation of 176 nT for non-STEVE  
 166 substorm events. The minimum SML values for these two categories of events differ by 122  
 167 nT on average. Both the official auroral electrojet indices or AL-index and the SuperMAG  
 168 variation referred to as the SML-index are examined in this study. Note that there are  
 169 several differences that exists between the two indices. For example, there is a total of 12  
 170 ground based magnetometer stations that are used for the official auroral electrojet indices  
 171 ( $AE = AU - AL$ ), whereas over 100 magnetometer stations in collaboration with SuperMAG  
 172 are used to derive the SuperMAG auroral electrojet indices ( $SME = SMU - SML$ ) (Newell  
 173 & Gjerloev, 2011). There is also a lack of AL-index data availability for events occurring  
 174 in 2018. The average minimum AL-index magnitude for STEVE events, excluding events  
 175 occurring in 2018, is -614 nT with a standard deviation of 192 nT, and the average minimum  
 176 AL-index magnitude for non-STEVE substorms is -519 nT with a standard deviation of 268  
 177 nT.

178 The substorm onset UT times, listed in Table 2, are identified in Newell and Gjerloev  
 179 (2011) using the satisfaction of the following SML criteria: the sharp initial SML drop  
 180 more than 45 nT in 3 minutes and the sustained SML drop (meaning 100 nT below the  
 181 average value for the duration of 25 minutes that starts 5 minutes after the onset). If these  
 182 conditions are met, the substorm onset is set at the last minute before a 15 nT drop in SML  
 183 (Newell & Gjerloev, 2011). Substorm phases have been identified by using the standard  
 184 definition according to the AL-index's slope (Kivelson & Russell, 1995). The growth phase  
 185 is typically identified by the initial interval of growing AL; while later, during the expansion  
 186 phase, AL rapidly decreases. Eventually AL reaches a minimum and then the index values  
 187 start increasing. This period of increasing AL is usually known as the substorm recovery  
 188 phase. An excellent example of the AL-index behaviour during substorms is presented in  
 189 Figure 13.19 of Kivelson and Russell (1995). It is important for the reader to remember  
 190 that, although SML index is calculated using more stations than the classical AL-index,  
 191 both indices represent the level of disturbance in the westward auroral electrojet recorded  
 192 by magnetometers.

## 193 2.2 Assimilative Mapping Analysis

194 The AMGeO procedure is used to generate assimilative maps of high-latitude electro-  
 195 dynamic variables by combining ground-based plasma drift and magnetic field observations  
 196 with empirical models of ionospheric convection and aurora (Cousins & Shepherd, 2010;  
 197 Newell et al., 2009) as described in Matsuo (2020). Assimilative maps of high-latitude elec-  
 198 trodynamics variables including electrostatic potential (ionospheric convection), Pedersen  
 199 and Hall conductance, and Joule heating are produced every 5 minutes for 3 hours for each  
 200 event listed in Section 2.1. Only AMGeO maps of electrostatic potential are presented in  
 201 this paper. These AMGeO electrostatic potential maps display equipotential contour lines,  
 202 marking convective motion of ionospheric plasma, in the geomagnetic latitudes and geomag-  
 203 netic local time coordinates, from 90 to 50 magnetic latitudes with geomagnetic local noon

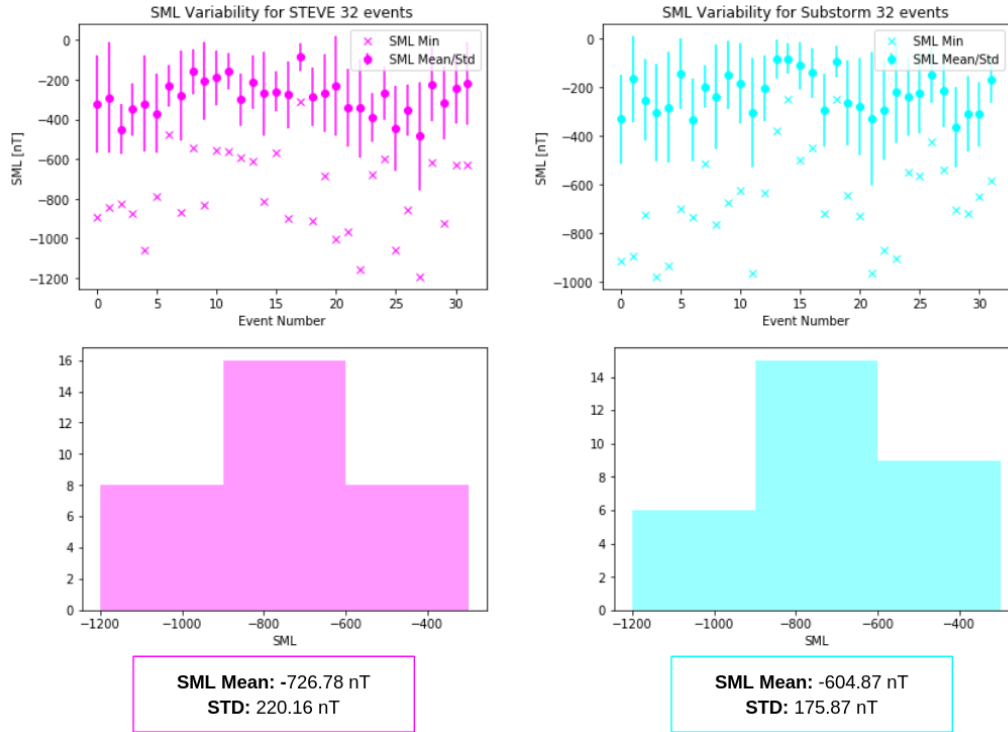


**Figure 2.** Top: Variability in the SML-index minimum and mean values for all 32 STEVE events (pink) and 32 non-STEVE substorm events (blue) Bottom: Histogram of SML-index minimum values for all 32 STEVE events (pink) and 32 non-STEVE substorm events (blue).

204 (12) at the top and midnight (0) at the bottom. The AMGeO’s spatial resolution is 2.5  
 205 degrees in latitude and 15 degrees in longitude. This is not high enough resolution to re-  
 206 solve narrow westward plasma flows usually associated with STEVE events in pre-midnight  
 207 subauroral latitudes, as shown for the SWARM ion drift (Figure 1 (c)).

208 The magnetic field observations ingested to AMGeO are ground-level magnetic per-  
 209 turbations from the SuperMAG data service which collects, standardize, and distribute  
 210 data from more than 300 ground-based magnetometers worldwide (Gjerloev, 2012). Addi-  
 211 tional data ingested include the line-of-sight ionospheric plasma drift observations from the  
 212 SuperDARN (Chisham et al., 2007). Ingesting ground-based magnetometer observations  
 213 into AMGeO requires an estimate of height-integrated ionospheric conductivity or conduc-  
 214 tance. Following McGranaghan et al. (2016), we used an optimal interpolation approach  
 215 to specify the Hall and Pedersen conductance. The data used for this purpose include  
 216 pseudo conductance observations created by DMSP SSJ particle precipitation as described  
 217 in McGranaghan et al. (2015). The conductance used for this study thus differs from the  
 218 default conductance maps used in AMGeO, which is derived from Ovation Prime electron  
 219 precipitation model (Newell et al., 2009).

### 220 2.3 Principal Component Analysis (PCA) and Superposed Epoch Analysis

221 To characterize global modes of variability of ionospheric convection associated with  
 222 STEVE as well as non-STEVE substorm events, AMGeO maps of electrostatic potential are  
 223 further analyzed using PCA. The mean convection map is first computed from assimilative  
 224 maps generated for the 32 STEVE events, which is then subtracted from each map to  
 225 generate residual maps. These residual maps are aggregated over time across all events and

**Table 2.** List of dates and UT onset time of 32 non-STEVE substorm events selected using the SuperMAG substorm database (Newell & Gjerloev, 2011).

Event	Date	Substorm Onset	Event	Date	Substorm Onset
1	2-11-2008	16:58	17	6-24-2011	7:09
2	3-26-2008	21:37	18	2-25-2012	11:26
3	2-11-2008	1:15	19	9-16-2013	14:46
4	3-12-2008	6:31	20	8-12-2014	20:14
5	3-18-2008	2:44	21	9-10-2015	16:29
6	3-10-2008	4:53	22	9-14-2015	15:01
7	4-6-2008	4:37	23	2-18-2016	2:56
8	3-10-2008	22:39	24	4-23-2016	21:03
9	3-29-2008	20:28	25	7-23-2016	5:01
10	3-12-2010	4:56	26	7-28-2016	4:05
11	3-20-2010	7:25	27	8-7-2017	8:18
12	4-7-2010	6:29	28	8-27-2017	15:53
13	4-8-2010	1:38	29	9-27-2017	12:14
14	9-9-2010	12:16	30	9-29-2017	11:25
15	9-15-2010	6:38	31	5-9-2018	4:26
16	4-24-2011	22:40	32	7-24-2018	5:45

Event dates with top 10 greatest minimum SML values are highlighted in red

used to compute a sample covariance that represents variability of ionospheric convection during STEVE events. The eigenvalue decomposition of this sample covariance matrix yields principal components as empirically determined eigenvectors. Each principal component is an independent orthogonal mode of variability from the mean. Principal components (PC) are ordered according to the percentage of variance that is attributed to each component. Once these global modes of variability of ionospheric convection are determined, the time-varying magnitudes of PC are computed from residual maps by linear regression, which are referred to as PC coefficients. The same PCA analysis steps are applied to assimilative maps generated for the 32 non-STEVE substorm events.

To examine the timing of temporal variation of PC coefficients and solar wind parameters and geomagnetic activity indices (including the AL-index, AU-index, IMF By and Bz parameters, and cross-polar cap potential), a correlation analysis and a superposed epoch analysis are further applied. Each time series, spanning from 1.5-hour prior to the STEVE optical onset (or substorm onset), to 1.5-hour post the STEVE optical onset (or substorm onset), is divided into quarter-hour increment bins. The center bin labeled at time zero is the bin in which the substorm onset time (or STEVE optical onset time) is included. The correlations between PC coefficients, AL-index, AU-index, IMF By/ Bz solar wind parameters, and cross-polar cap potential are computed using the spearman correlation function from the Python SciPy library. Aurora electrojet indices (AL and AU index), and Interplanetary Magnetic Fields (IMF) By and Bz obtained from OMNI database at 1-minute cadence are used.

### 3 Data Analysis Results

This section presents both quantitative and qualitative analysis results of AMGeO electrostatic potential maps obtained for 32 STEVE events and 32 non-STEVE substorm events as described in Section 2. These analysis results help characterize global high-latitude ionospheric convection features associated with STEVE events and non-STEVE substorm events. Section 3.1 introduces representative features of the dawn-dusk asymmetry or dawn-

cell extension found, in a varying degree, among individual 32 STEVE events. Differences in the mean convection patterns and cross-polar cap potential are evaluated between the two categories of events in Section 3.2. In Section 3.3 the dawn-cell extension morphology observed in AMGeO maps is further examined in terms of the leading modes of global ionospheric convection variation associated with STEVE events as well as correlation of each mode’s amplitude with solar wind parameters, and geomagnetic indices. Section 3.4 investigates the same for non-STEVE substorm events in order to contrast the differences in the ionospheric convection’s characteristic behaviors found for 32 STEVE events from those behaviours identified for 32 non-STEVE substorm events that occur without the presence of STEVE. The median PC coefficient trend, that represents a typical temporal variation of these modes for all 32 STEVE and 32 non-STEVE substorm events, as well as the electrostatic potential maps reconstructed with the PC and median PC coefficient for both categories of events are described in Section 3.5. In addition to typical temporal behaviors of leading modes, Section 3.6 further investigates the dawn-cell extension and evaluates the temporal trends of PC coefficients and AMGeO electrostatic potential maps for 10 individual STEVE and 10 non-STEVE substorm events. A case study for STEVE event occurring on March 26, 2008 and its comparison to a non-STEVE substorm event occurring on September 14, 2015 are presented in Section 3.7. An overall comparison of characteristic features of high-latitude electrodynamics between STEVE events and non-STEVE substorm events is summarized in Section 4.

### 3.1 Dawn-Dusk Asymmetric Ionospheric Convection Patterns Found in STEVE Events

For 27 of the 32 STEVE events investigated, a strong dawn-cell extension, identified as the westward penetration of the dawn cell into the pre-midnight sector in the vicinity of subauroral latitudes, is observed in the AMGeO maps. An example of an AMGeO spatial distribution map displaying this strong dawn-cell extension during a STEVE event can be viewed in Figure 3. Four of the 32 STEVE events have displayed a weaker dawn-cell extension. Specific STEVE event dates that displayed a weak dawn-cell extension can be found in Supplemental Materials Table S1. There is a dawn-cell extension associated with non-STEVE substorm events (Section 3.4), however the magnitude and morphology differences of this feature make it distinguishable from STEVE events. It should be noted that in the context of this study subauroral latitudes indicate magnetic latitudes below about 70 degrees and the term “subauroral latitudes” is not referring to the auroral boundaries defined by precipitating auroral particles. As noted in the introduction, AMGeO cannot resolve the narrow fast flows of ion drifts directly associated with STEVE. The focus is therefore rather on the localised convection patterns with a reminiscence to the Harang reversal wherein that is spatially collocated with STEVE optical emissions.

### 3.2 Mean Ionospheric Convection for STEVE and non-STEVE Substorm Events

The mean convection pattern is estimated for each category of events from AMGeO maps produced at 5-minute cadence for each 3-hour duration of all 32 STEVE and 32 non-STEVE substorm events. Figure 4 (a) is the mean convection pattern for STEVE events, with a cross-polar cap potential of 48.15 kV, and shows the dawn cell slightly extending past the midnight boundary into the pre-midnight sector between 75 and 65 degrees magnetic latitude. In comparison, Figure 4 (b) shows the mean convection pattern for non-STEVE substorm events. The mean convection pattern for non-STEVE substorm events is noticeably weaker than the mean convection found for STEVE events, with a cross-polar cap potential of 39.32 kV. The extension of the dawn cell observed in the mean convection pattern for STEVE events is also slightly more prominent and further extending into the pre-midnight sector. The physical implications of this enhanced electrostatic potential during STEVE-events is addressed later in Section 5.

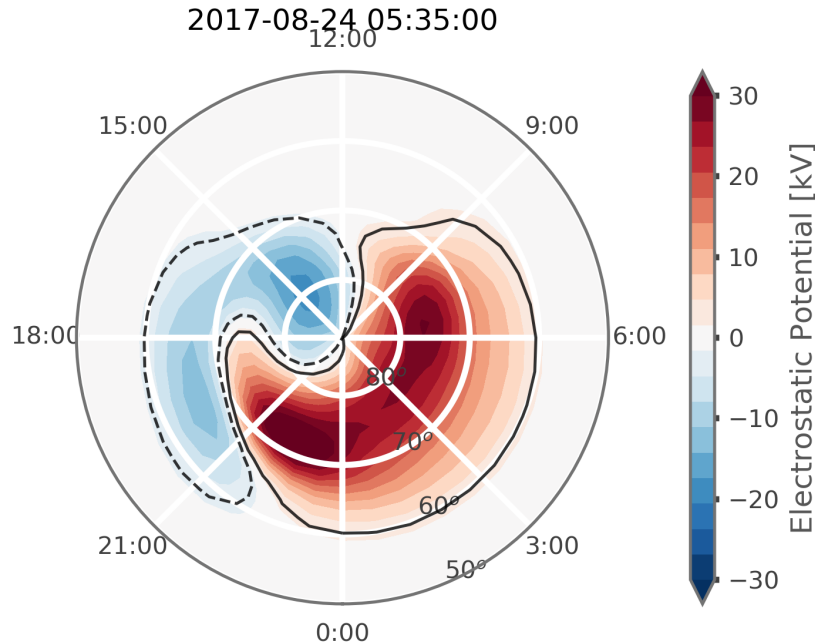


**Figure 3.** AMGeO map for STEVE event occurring on August 8th, 2017 at 5:35 UT that displays a strong dawn-cell extension penetrating into the dusk cell, reaching past the pre-midnight sector, near subauroral latitudes.

### 3.3 Global Modes of Ionospheric Convection Variability Associated with STEVE Events

A strong dawn-cell extension observed in the majority of the STEVE events, as introduced in Section 3.1), is further examined in terms of the global modes of variability about the mean convection pattern shown in Figure 4 (a) in Section 3.2. Figure 5 displays the maps of the first four modes, noted here as PC1 through PC4. The map of PC1 (Figure 5 (a)) appears to be a dawn-cell intensification mode and explains 51.6 percent of the total variance of the ionospheric convection assimilative maps estimated for 32 STEVE events. PC2 (Figure 5 (b)) also has a significant explained variance of 23.4 percent, and its two-cell pattern shows a dawn-cell penetrating into the dusk cell around 65 degrees magnetic latitude in the pre-night sector, characterizing a localized nightside dawn-cell penetrating mode. PC3 (Figure 5 (c)) exhibits a considerable nightside asymmetrical pattern which seems to correspond to a mode of variability associated with the dawn cell extending very far westward into and past the pre-midnight sector. PC3 is thus referred to as the dawn-cell extension mode or STEVE mode and has an explained variance of 7.9 percent. PC4 has low explained variance, contributing less than 5 percent of the overall variance in all STEVE events and is referred to as a weak asymmetry mode. Among these four principal components, PC2 and PC3 (Figure 5 (b)-(c)) are of particular interest for this study as these modes visually represent the westward dawn-cell extension into the pre-midnight sector.

Superposed epoch analysis of time-varying PC coefficients and cross-polar cap potential is shown in the pink colored box-plots in Figure 6 over 1.5 hour prior to and 1.5 hour post substorm onset. Superposed epoch analysis of AL-index, AU-index, IMF By, and IMF Bz is included to examine the relationship of global modes of ionospheric convection evolution to solar wind drivers and overall substorm evolution indicated by geomagnetic indices. The

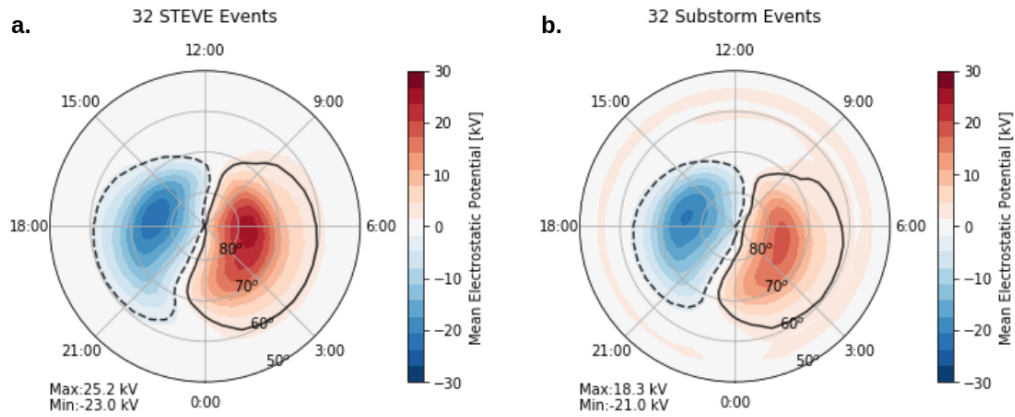


**Figure 4.** a.) Mean electrostatic potential distribution from 32 STEVE events. The cross-polar cap potential is 48.15 kV. The maximum and minimum potential values are 25.2 kV and -23.0 kV, respectively. b.) Mean electrostatic potential distribution produced using 32 non-STEVE substorm events. The cross-polar cap potential was calculated to be 39.32 kV. The maximum and minimum potential values are 18.3 kV and -21.0 kV, respectively

328 correlations between PC coefficients, AL-index, AU-index, IMF By, IMF Bz, and cross-  
 329 polar cap potential are summarized in Figure 7. IMF, AL and AU are obtained from the  
 330 NASA OMNI database. The median of PC1 coefficients changes signs from negative to  
 331 positive close to the time of substorm onset marked by the blue vertical line at 0.0 hour  
 332 (Figure 6 (a)). At the time of this sign change there is also an intensification observed in the  
 333 magnitude of the dawn cell in terms of electrostatic potential values which can be visualized  
 334 in Section 3.5 Figure 11.

335 There is a significant negative correlation at -0.65 between PC1 coefficient and IMF  
 336 By, so the changes of PC1 mode are partly attributed to the changes of IMF By. The  
 337 median of PC2 coefficients, representing a localized nightside dawn cell penetrating mode,  
 338 maximizes at the time of substorm onset (Figure 6 (b)). The median of PC3 STEVE mode  
 339 coefficients also changes signs, close to the substorm onset, from negative to positive (Figure  
 340 6 (c)). The median of PC3 coefficients reaches its maximum at 0.5 hour post substorm onset,  
 341 corresponding to the time when the dawn-cell extends into the pre-midnight sector most.  
 342 This coincides with the end of expansion phase and beginning of recovery phase as well as  
 343 with the time of the STEVE optical onset, which is consistent with the STEVE onset timing  
 344 reported in GallardoLacourt et al. (2018).

345 The median magnitude of IMF By and Bz is very small and predominantly negative  
 346 for the entire 3-hour duration of superposed epoch analysis (see Figure 6 (g)-(h)). The  
 347 superposed epoch analysis of AL-index (Figure 6(e)) shows that the minimum of median AL  
 348 at -410 nT occurs 0.5 hour after the substorm optical onset, marking the end of expansion  
 349 phase and beginning of recovery phase. The median cross-polar cap potential is seen to  
 350 maximize at 62.8 kV, at 0.5 hour post substorm onset in the recovery phase (Figure 6 (f)).  
 351 The cross-polar cap potential also has significant negative correlation with PC1 coefficient  
 352 of -0.67 and with PC2 coefficient of 0.66 (Figure 7). The AL-index negatively correlates  
 353 with PC2 coefficient at -0.53, and PC3 shows a small negative correlation of -0.28 to the  
 354 AL index. The STEVE mode associated with the dawn-cell extension (PC3) has no other  
 355 significant correlations, except for a slight positive correlation to IMF Bz at 0.21. This  
 356 dawn-cell extension is found to be unrelated to IMF By, which is largely in agreement

with the past studies. For instance, the previous work using SuperDARN data have found that a typical IMF By dependent dawn-dusk asymmetry is seen over the entire convection pattern during the substorm growth phase but during the expansion phase this asymmetry is confined only in the polar cap and dayside (Grocott et al., 2010).

The average duration of the optical STEVE phenomenon in the 32 events investigated is found to be 1 hour with a standard deviation of 34 minutes. For the 27 STEVE events with a detectable strong dawn-cell extension in the pre-midnight sector, the average optical STEVE event duration is 1 hour 16 minutes. These are largely consistent with the STEVE duration of 1 hour as reported in GallardoLacourt et al. (2018). The dawn-cell extension found from these 27 events lasts 1 hour and 12 minutes on average, which is about the same duration of optical STEVE events. Note that no apparent event-by-event correlation is found between the durations of the dawn-cell extension and the optical STEVE event, even though the average durations are similar.

### 3.4 Global Modes of Ionospheric Convection Variability Associated with Non-STEVE Substorms

Figure 8 shows the first four leading global modes of variability for 32 non-STEVE substorms events. These modes represent spatially coherent variability about the mean convection pattern shown in Figure 4 (b). The PC maps for the non-STEVE substorm events are generally similar to the PC maps for STEVE events (Figure 5 (a)-(d)) with the exception of PC3. PC1 represents a dawn-cell intensification mode like PC1 for STEVE events, and has an explained variance of 46.3 percent and shows significant correlation to IMF By and Bz (Figure 10). PC2 has an explained variance of 25.2 percent and shows a two-cell spatial distribution with the dawn cell penetrating into the dusk cell in the pre-midnight sector in a similar fashion to the localized nightside dawn-cell penetrating mode found for STEVE events (Figure 8 (b)). PC3 appears to represent a dawn-cell extension mode for non-STEVE substorms (Figure 8 (c)), exhibiting an asymmetrical pattern associated with the dawn-cell westward extension into the pre-midnight sector on nightside. However, a close inspection of PC3 for non-STEVE substorm events, which has an explained variance of 7.2 percent, shows that the extent of dawn-cell extension is not as prominent as PC3 for STEVE events (Figure 5 (c)). PC4 has the lowest explained variance contributing about 5 percent of overall variance in all non-STEVE substorms events and is referred to as a weak asymmetry mode (Figure 8 (d)).

Superposed epoch analysis of the PC coefficients, AL-index, AU-index, IMF By and Bz, and cross-polar cap potential for non-STEVE substorm events are shown in the blue colored box-plots shown in Figure 9. The blue vertical line at 0.0 hour marks the substorm onset at when superposed epoch analysis is centered. PC coefficients for the substorm events are correlated to solar wind parameters and geomagnetic activity indices in the same manner as for STEVE events (Figure 10). In the superposed epoch analysis, the median of PC1 coefficients for 32 non-STEVE substorm events is seen to change signs from negative to positive around the time of substorm onset (Figure 9 (a)). The median of PC2 coefficients, representing a localized nightside dawn-cell penetrating mode of variation, maximizes slightly after time of substorm onset around 0.25 hour (Figure 9 (b)). The median of PC3 coefficients change signs close to the substorm onset going from negative to positive (Figure 9 (c)). The timing of the maximum of PC3 coefficients directly corresponds to the peak of dawn-cell extensions into the pre-midnight sector as confirmed in the electrostatic potential maps.

The median of IMF By is very small in magnitude and predominantly positive for the 3-hour duration of the superposed epoch analysis (Figure 9 (g)). Note that the median of IMF By is predominantly negative for STEVE events (Figure 6 (g)). The median IMF Bz varies from nearly zero at 1.5 hour prior to onset and decreases to about -3 nT at substorm onset followed by the slow return to zero over 1.5 hours post substorm onset (Figure 9 (h)).

408 The temporal trends of  $B_y$  and  $B_z$  over the 3-hour duration of superposed epoch analysis  
 409 are generally smoother for non-STEVE substorm events in comparison to STEVE events.  
 410 There is notable negative correlation between PC1 coefficient and IMF  $B_y$  (-0.62) and  
 411 between PC1 coefficient and IMF  $B_z$  (-0.44). The AL magnitude for non-STEVE substorm  
 412 events is smaller when compared to STEVE events. These results are consistent with the  
 413 superposed epoch analysis of the AL-index from GallardoLacourt et al. (2018) in which  
 414 the AL magnitude for STEVE events was observed to be higher than observed for regular  
 415 non-STEVE substorms. The cross-polar cap potential for non-STEVE substorm events is  
 416 also significantly weaker in magnitude across the 3-hour duration of the superposed epoch  
 417 analysis compared to STEVE events.

### 418 **3.5 Reconstructed Ionospheric Convection Maps for STEVE and Non-STEVE** 419 **Substorm Events**

420 The mean convection map, PC maps, and the median values of PC coefficients, de-  
 421 scribed in Sections 3.2-3.4, are used to reconstruct a time series of electrostatic potential  
 422 maps at 0.5 hour cadence over 3 hours from 1.5-hour prior through 1.5-hour post substorm  
 423 onset time for both categories of events. The median values for PC coefficients are also  
 424 graphed relative to substorm onset time to investigate temporal trends in global ionospheric  
 425 convection patterns and to identify the differences between two categories of events as shown  
 426 in Figure 11, from the top to bottom, at three key time frames at 30 minutes before and  
 427 after as well as at time of substorm onset. These reconstructed ionospheric convection maps  
 428 reflect typical spatiotemporal variability of convection patterns derived from the results of  
 429 PCA and superposed epoch analysis of AMGeO maps, and provide helpful insight into the  
 430 timing and duration of the dawn-cell extension development relative to substorm onset.  
 431 Black contour lines are added to demarcate the boundaries of positive and negative cells in  
 432 order to aid in the visualization of the dawn-cell extension into the pre-midnight sector.

433 Prior to the substorm onset time, there is a slight westward extension of the dawn cell  
 434 visible for both STEVE and non-STEVE substorm events (Figure 11 (top)). At this time,  
 435 PC1-PC3 coefficients are all growing in magnitude for both STEVE and non-STEVE events.  
 436 At substorm onset, shown in Figure 11 (middle), there is a change in the sign of PC1 and  
 437 PC3 coefficients relating to an intensification of the dawn cell as observed in reconstructed  
 438 electrostatic potential maps for both categories of events. The enhancement of the dawn cell  
 439 is noticeably greater in magnitude for STEVE events compared to non-STEVE substorm  
 440 events. Figure 11 (bottom) displays maps reconstructed at 30 minutes after substorm onset.  
 441 The median value of PC3 coefficients peaks at this time which is the point of the greatest  
 442 dawn-cell extension among three time frames shown in Figure 11. The dawn-cell extension  
 443 into the pre-midnight sector for STEVE events is more pronounced more clearly extending  
 444 into the dusk cell, whereas the dawn-cell extension for non-STEVE substorm events is  
 445 visibly weaker in magnitude. The temporal trend of PC1 coefficients after substorm onset  
 446 is distinctively different for STEVE and non-STEVE substorm events. For non-STEVE  
 447 substorm events all PC coefficients, including PC1 (dashed red line,) are approaching zero  
 448 reflecting the return of a symmetric two cell convection pattern towards the end of the  
 449 recovery phase. For STEVE events the median values of PC2, PC3, and PC4 coefficients  
 450 all approach or reach zero after one hour post substorm onset. However, the median of PC1  
 451 coefficients (solid red line) continues to grow even after substorm onset, contributing to  
 452 the prolonged dawn-dusk asymmetry on nightside visible in convection patterns for STEVE  
 453 events.

### 454 **3.6 Dawn-cell Extension in Individual STEVE and Non-STEVE Substorm** 455 **Events**

456 The dawn-cell extension is further investigated by closely evaluating the temporal trends  
 457 of PC coefficients and AMGeO electrostatic potential maps for 10 STEVE and 10 non-  
 458 STEVE individual substorm events that are selected based on the peak magnitude of min-

imum SML values (see event dates denoted in red for STEVE events in Table 1 and for non-STEVE substorm events in Table 2). Figure 12 shows AMGeO electrostatic potential maps for these 10 STEVE events at the time the greatest dawn-cell extension suggested by the maximum time of PC3 coefficients. A strong dawn-cell extension is visible in the pre-midnight sector near subauroral latitudes for 9 out of the 10 events except for the STEVE event occurring on February 8, 2016 (Figure 12 (f)).

The temporal trends observed in PC coefficients of these 10 individual STEVE events are consistent with the overall trends seen in the median of PC coefficients for all 32 STEVE events (Figure 6). For these 10 events, the magnitude of PC1, which is characterized as the dawn-cell intensification mode in Section 3.3, exhibits a strong negative correlation with IMF By at -0.71 with the sign changes coinciding with changes in the IMF By orientation. The overall temporal evolution of PC1 coefficients for the 10 events is also related to AL and IMF Bz as for all 32 STEVE events (Figure 7). PC1 coefficients increase in magnitude prior to substorm onset during the growth phase for all 10 events, and do not approach or reach zero during the recovery phase for 7 out of 10 events. In addition, in 9 out of 10 events, there is a significant amount of dawn-dusk asymmetry with a dawn-cell extending into the pre-midnight sector about 1.5 hours after substorm onset, well into the recovery phase. The localized nightside dawn-cell penetrating mode (PC2) is also seen to increase during the growth phase prior to substorm onset and has some correlation with IMF Bz, IMF By and AL at -0.47, 0.34, -0.49. See Figure 7 for correlation for all 32 STEVE events. Correlation matrix and superposed epoch analysis for 10 STEVE events with strongest SML is provided in supplementary material. The peak time of PC2 coefficients for these individual events has a lot of variability, for 6 out of 10 events occurring in the expansion phase and for 4 of 10 events occurring in the recovery phase. The AMGeO electrostatic potential maps at the time of PC2 coefficient maximum show a strong dawn-dusk asymmetry in 10 out of the 10 events, similar to the morphology of PC2 (Figure 5 (b)) where the dawn cell is extended past the midnight boundary penetrating the dusk cell. The primary mode of variability associated with the westward extension of the dawn-cell into the pre-midnight sector is PC3 as seen in the morphology of AMGeO electrostatic potential maps shown at the time of PC3 coefficients' maximum in Figure 12 (a-e, g-h). The magnitude of PC3 grows in magnitude prior to substorm onset for all 10 events, and continues into the recovery phase for some events. The PC3 coefficient peak time has some variability for individual events, but for the majority (7 out of 10 events) the maximum of PC3 coefficient occurs in the recovery phase and for the remaining events it occurs during the expansion phase. There are no notable temporal trends of the magnitude of PC4 that is the weak asymmetry mode, as the coefficients are small in magnitude and remain largely close to zero.

There are differences and similarities between these individual STEVE events and non-STEVE substorm events in terms of the morphology of ionospheric convection patterns at the time of PC3 coefficient peak and temporal evolution of PC1-PC4 coefficients. One of the most notable differences is that the dawn-cell extension for non-STEVE substorm events is typically not as far extended into the pre-midnight sector as for STEVE events, more localized around midnight. It typically lasts from the growth phase through the end of expansion phase, fading completely by the end of expansion phase for 7 out of 10 non-STEVE substorm events. For these 10 non-STEVE substorm events, PC1 coefficients have a strong negative correlation with IMF By and IMF Bz at -0.43 and -0.53, respectively. See Figure 10 for correlation for all 32 non-STEVE substorm events. Correlation matrix and superposed epoch analysis for 10 non-STEVE substorm events with strongest SML is provided in supplementary material. As for 10 STEVE events, PC1 coefficients increase in magnitude more rapidly during the substorm onset or right after onset during the expansion phase for all 10 events. Unlike for STEVE events, PC1 coefficients typically approach or reach zero during the recovery phase, returning to a symmetrical two-cell convection patterns about 1.5 hours after the substorm onset during the recovery phase (7 out of 10 non-STEVE substorm events). PC2 coefficients increase in magnitude during the growth phase prior to the substorm onset and has some correlations to IMF Bz, IMF By, and AL at -0.30, 0.40, -

513 0.41. This behavior is similar between individual STEVE and non-STEVE substorm events.  
 514 The peak time of PC2 coefficients has a lot of variability among these 10 events, occurring in  
 515 the growth phase for 3 out of 10 events, in the expansion phase for 4 out of 10 events, and in  
 516 the recovery phase for 3 of 10 events. The AMGeO electrostatic potential maps at the time  
 517 of PC2 coefficient maximum show a strong dawn-dusk asymmetry in 10 out of 10 events  
 518 in a similar fashion to STEVE events. Unlike STEVE events, the PC3 coefficients increase  
 519 in magnitude post substorm onset for non-STEVE substorm events. The PC3 coefficient  
 520 peak time has some variability among individual events, but for the majority (6 out of 10  
 521 events) PC3 coefficients reaches their peak at the end of the expansion phase. For the  
 522 remaining events, it occurs during the beginning of the recovery phase. The morphology of  
 523 AMGeO electrostatic potential maps at the time of PC3 coefficients maximum has a dawn-  
 524 cell extension into the pre-midnight sector in 10 out the 10 events as shown in Figure 13.  
 525 The maximum of PC3 coefficients correlates to the maximum of dawn cell intensification  
 526 and westward extension. It can be noted that this dawn cell extension is less pronounced  
 527 and more diversified when compared to the dawn cell morphology observed in STEVE  
 528 events. As for STEVE events, there is nothing notable aspects about PC4 coefficients for  
 529 individual non-STEVE events. See Figure 9) for the overall temporal trends of the median  
 530 PC coefficients for all 32 non-STEVE substorm events.

### 531 **3.7 Case Study Events: STEVE Event March 26, 2008 vs non-STEVE Sub-** 532 **storm Event September 14, 2015**

533 Key differences in global high latitude electrodynamics between STEVE and non-  
 534 STEVE substorm events are discussed for two specific case study events: the STEVE event  
 535 occurred on March 26, 2008 (Figure 14) and the non-STEVE substorm event occurred on  
 536 September 14th, 2015 (Figure 15). These events are chosen for comparison as they have  
 537 similar SML minimum values. In addition, this STEVE event has been investigated in detail  
 538 by Nishimura et al. (2020).

539 The AMGeO electrostatic potential maps for the STEVE event on March 26th, 2008  
 540 are shown in Figure 14, from 6:00 UT to 9:15 UT in 5-minute intervals during the STEVE  
 541 optical event (from 7:20 UT to 8:00 UT) otherwise in 15-minute intervals, with maps at  
 542 substorm onset at 6:30 UT as marked with a black dotted box and at STEVE optical onset  
 543 at 7:20 UT marked with a pink dotted box. The SML minimum value for this event is -826  
 544 nT at 7:20 UT, occurring at the end of the expansion phase and the beginning of the recovery  
 545 phase, which is indicated by a black solid box. A slight westward extension of the dawn cell  
 546 can be observed at 6:00 UT. As time progresses the dawn cell becomes more enhanced and  
 547 extending further into the pre-midnight sector. The maximum of the dawn-cell extension,  
 548 which occurs when PC3 coefficients are maximized, can be seen at 7:20 UT, which is also  
 549 the STEVE optical onset and beginning of substorm recovery phase. After reaching the  
 550 maximum, the magnitude of the dawn-cell extension decreases and a mostly symmetric two  
 551 cell convection pattern can be observed 1 hour and 25 minutes into the recovery phase at  
 552 8:45 UT.

553 For comparison, the AMGeO electrostatic potential maps for the non-STEVE substorm  
 554 event on September 14th, 2015 are shown in Figure 15 from 14:00 UT to 17:15 UT. Maps  
 555 are displayed in 15 minute intervals from 14:00 UT through 15:00 UT prior to substorm  
 556 onset and from 16:00 UT through 17:15 UT after substorm onset and in 5 minute intervals  
 557 otherwise, with maps at the substorm onset (15:00 UT) marked with a black dotted box and  
 558 at the time of SML minimum (15:40 UT) marked with a black solid box in Figure 15. The  
 559 SML minimum value for this event is -935 nT. Here, there is also a slight and weak extension  
 560 of the dawn cell present one hour prior to the substorm onset at 14:00 UT. The dawn cell  
 561 extension becomes more prominent as time progresses but it is not as far extended into the  
 562 pre-midnight sector as observed for the STEVE event in Figure 14. The maximum time of  
 563 the dawn cell extension occurs at the PC3 coefficient maximum at 15:40 UT. After this time  
 564 the dawn cell extension decreases and a more dawn-dusk symmetric convection pattern is

565 observed approximately 50 minutes into the recovery phase of the substorm at 16:30 UT.  
 566 In this non-STEVE substorm event, the dawn cell extension has a shorter duration than  
 567 that observed for the STEVE event. The potential physical implications of this difference  
 568 is addressed later in the discussion section.

569 Upon a visual inspection, the westward extension of the dawn cell that is present in  
 570 AMGeO electrostatic potential maps for the STEVE event on March 26, 2008 shows a  
 571 resemblance in its shape and location to the westward surge reported by Nishimura et  
 572 al. (2020) for the same STEVE event. Nishimura et al. (2020) have concluded that for  
 573 STEVE events the intense upward field-aligned currents and substorm surge reach further  
 574 into the dusk sector, while for non-STEVE substorms are localized at midnight (Nishimura  
 575 et al., 2020). Both of the STEVE events included in the Nishimura et al. (2020) study are  
 576 in fact included in the list of 32 STEVE events investigated in this study. The AMGeO  
 577 convection patterns for March 26, 2008 and April 5, 2010 both displayed a strong dawn-cell  
 578 extension. Qualitative similarities are observed between the westward dawn-cell extension  
 579 and the westward substorm surge seen in results from Nishimura et al. (2020). From a  
 580 visual comparison of AMGeO electrostatic potential maps for these two events, the dawn  
 581 cell extension appears more prominent in the event occurring on March 26, 2008. This is  
 582 consist with the DMSP Special Sensor Ultraviolet Spectrographic Imager (SUSSI) Lyman-  
 583 Birge-Hopfield long (LBHL) data and the results presented by Nishimura et al. (2020) in  
 584 which the event on March 26, 2008 appears to have a more intense substorm surge than the  
 585 event occurring on April 5, 2010.

#### 586 **4 Summary of Comparisons between STEVE and non-STEVE Substorm** 587 **Events**

588 This section provides four tables that summarize the data analysis results presented  
 589 in Section 3 and compare the key differences identified between STEVE and non-STEVE  
 590 substorm events. Table 3 explains the morphological and timing differences in the dawn cell  
 591 extension observed in AMGeO convection maps between STEVE and non STEVE substorm  
 592 events. In Table 4 comparisons of PCA results are summarized between both categories of  
 593 events. Magnitude differences in cross-polar cap potential and IMF By and IMF Bz are  
 594 discussed in Table 5 and Table 6, respectively.

**Table 3.** Summary of the key differences in the dawn-cell extension observed in STEVE and non-STEVE substorm events

<b>Dawn Cell Extension</b>	
<b>STEVE events</b>	<b>Non-STEVE substorm events</b>
The dawn cell extension typically extends farther into the pre-midnight sector (Sections 3.6-3.7).	The dawn cell extension is mostly not as far extended into the pre-midnight sector, localized around midnight (Sections 3.6-3.7).
Significant dawn-cell extension is present from the growth through recovery phase for 9/10 events (Section 3.6). Typical behaviours among 32 events are the same (Section 3.5).	Significant dawn-cell extension is present from the growth to end of expansion phase for 7/10 events (Section 3.6). Typical behaviours among 32 events are the same (Section 3.5).

## 5 Discussion

In Table 1 in Section 2.1 the STEVE optical onset time in UT for the 32 STEVE events investigated in this study are defined. It should be noted that there are some ambiguities associated with the definition of these STEVE onset times. As reported by (GallardoLacourt et al., 2018), the STEVE optical onset is defined as the time when STEVE is first observed within the field-of-view of a ground-based auroral imager. Since STEVE is a westward moving structure, it is possible that STEVE forms further eastward resulting in a time difference between the initial appearance of STEVE and its detection by an ASI. Nevertheless, STEVE propagates rapidly westward potentially, so discrepancies may be on the order of minutes. This study also utilizes the substorm onset times obtained from the SuperMAG substorm database for the 32 non-STEVE substorm events investigated (Table 2). The substorm onset times in the SuperMAG dataset are defined using the technique presented in Newell and Gjerloev (2011). There are different definitions of substorm onset timing depending on the technique or method used for substorm onset identification (e.g., Frey et al. (2004); Nishimura et al. (2010); Forsyth et al. (2015)).

Regarding the physical implications of the Harang Reversal, previous studies on ionospheric convection patterns [e.g., Grocott et al. (2010); Kamide and Kokubun (1996); Zou et al. (2009)] have shown a relationship between the dawn-dusk asymmetry in the electrostatic potential, substorms, and the formation of the Harang discontinuity or Harang reversal. Specifically, Grocott et al. (2010) reported that the IMF strongly governs the behaviour of this asymmetry during the substorm growth phase; however, this asymmetry was not maintained around magnetic midnight during the expansion phase. This result is consistent with our analysis of 32 substorm events without the presence of STEVE. By contrast, for the 32 STEVE events the asymmetric nature of the electrostatic potential pattern is strong even during the recovery phase, after STEVE is optically observed. As reported by GallardoLacourt et al. (2018), the STEVE events analyzed here do not exhibit an IMF dependence.

In addition, this asymmetry has been known to be associated with the formation of the Harang reversal. Harang (1946) originally named it *Harang discontinuity* based on the ground-based magnetometer observations showing the directional change in magnetic field perturbations in the region. The Harang reversal thus corresponds to the location where the eastward electrojet overlaps with the westward electrojet and represents a region of converging electric fields in the nightside ionosphere at auroral latitudes. More broadly, the Harang reversal can be considered in terms of a convection structure where the two auroral electrojets overlap. This study adopts the Harang reversal definition in terms of ionospheric convection structure features, similarly to Ohtani et al. (2016), instead of its original definition based on ground magnetic disturbances. Some physical insights into this high-latitude ionospheric convection structure can be gained from the work by Gkioulidou et al. (2009). They have investigated electrodynamic processes involved in the Harang reversal's formation and reported that the equatorward portion of the convergent electric fields (associated with the Harang reversal) contribute to intensify the initial poleward electric field in that region, producing strong westward subauroral  $\mathbf{E} \times \mathbf{B}$  drifts identified as SAPS. As previously mentioned, this study reveals that the asymmetric electrostatic potential patterns observed for regular substorms in absence of STEVE is mainly observed during the growth and expansion phase of substorm. In contrast, for the STEVE events studied in this paper, the asymmetric mode of variability starts to form during the substorm growth phase and is maintained well into the recovery phase beyond STEVE optical onset. Considering the results reported by Gkioulidou et al. (2009), this study's results suggest that the Harang reversal is present for a longer time during STEVE events than regular substorms, potentially playing a role in enhancing even further westward subauroral  $\mathbf{E} \times \mathbf{B}$  drifts. This mechanism could help explain the connection between STEVE and extreme SAIDs previously reported in Archer et al. (2019a); MacDonald et al. (2018).

647 Furthermore, a recent study by Nishimura et al. (2020) has reported on the magne-  
 648 topheric conditions for two STEVE events and compared to conditions found during two  
 649 non-STEVE SAID/SAPS substorm events. Using SUSSI images from DMSP satellites, they  
 650 have found that for STEVE events the substorm surge and intense upward field-aligned cur-  
 651 rents, reaching into the pre-midnight dusk sector, but for non-STEVE substorms they are  
 652 localized around midnight. Although more research is needed to clearly elucidate this, the  
 653 electrostatic potential asymmetry identified in this study could help explain the surge's  
 654 fast motion reported by Nishimura et al. (2020). The two STEVE events included in the  
 655 Nishimura et al. (2020) investigation are the March 26, 2008 and April 5, 2010 events, which  
 656 are also investigated in this paper. The dawn-cell extensions seen in the AMGeO convection  
 657 patterns produced for these events display qualitative similarities to the westward substorm  
 658 surge extension reported in Nishimura et al. (2020) (see Supplementary Material Movie 1  
 659 and Movie 2 for more information). From a comparative visual inspection of the AMGeO  
 660 convection patterns for the STEVE events occurring on March 26, 2008 and April 5, 2010,  
 661 the westward extension of the dawn cell appears more prominent for the event occurring  
 662 on March 26, 2008. This is in agreement with the DMSP's SUSSI LBHL image analysis  
 663 presented by Nishimura et al. (2020). Physical implications of the potential connection be-  
 664 tween the dawn-cell extension trend found in AMGeO electrostatic potential maps in this  
 665 study and the substorm surge identified in SUSSI images in Nishimura et al. (2020) may be  
 666 further investigated in the future; however, it should be noted that there are differences in  
 667 terms of the data being used and the scales of interests between these studies.

## 668 6 Conclusions

669 This paper presents the first comprehensive study focusing on characteristic global-scale  
 670 ionospheric electrodynamics associated with STEVE events and identifies key differences  
 671 from non-STEVE substorm events. We have found distinguishing differences in the mean  
 672 convection patterns and global modes of convection patterns variability around the mean for  
 673 these categories of events. This data-intensive STEVE study involves 192 total hours of  
 674 5-minute assimilative mapping analysis by AMGeO. These assimilative mapping analysis of  
 675 high-latitude ionospheric convection patterns are obtained from a large amount of Super-  
 676 DARN plasma drift data and ground-based magnetometer data distributed by SuperMAG  
 677 for 32 STEVE and 32 non-STEVE substorm events. The PCA, superposed epoch analysis,  
 678 and correlation analysis are further applied to the AMGeO maps to identify key differences  
 679 between STEVE and non-STEVE substorm events as summarized in Section 4. In general,  
 680 our findings are consistent with the previous studies by GallardoLacourt et al. (2018) and  
 681 Nishimura et al. (2020) suggesting that STEVE optical events occur during specific and  
 682 unique types of substorms that are distinct from typical substorms where STEVE is not  
 683 present.

684 Main findings regarding specific differences in the global convection patterns observed  
 685 during substorms with and without STEVE events are categorized into four main categories  
 686 including magnitude, morphology, and timing as well as the relationship to geomagnetic  
 687 activity parameters described below.

### 688 Magnitude

- 689 • A magnitude difference in cross-polar cap potential drop observed in the mean electro-  
 690 static potential maps for STEVE and non-STEVE substorm events is about 10 kV.  
 691 For STEVE events the magnitude is 48.15 kV compared to non-STEVE substorm  
 692 events at 39.32 kV (Section 3.2).
- 693 • A larger magnitude of cross-polar cap potential is present across the entire 3-hr du-  
 694 ration of the superposed epoch analysis for STEVE events compared to non-STEVE  
 695 substorm events (Sections 3.3 and 3.4).

### 696 Morphology

- 697 • There is also a difference in the dawn-cell extension morphology between STEVE and  
698 non-STEVE substorm events. For the majority of the 32 STEVE events investigated  
699 in this study, a strong westward extension of the dawn cell, penetrating into the dusk  
700 cell in the pre-midnight sector near subauroral latitudes, is observed (Section 3.1).
- 701 • A dawn cell extension is also observed in the AMGeO electrostatic potential maps  
702 of non-STEVE substorm events; however, the dawn cell morphology is typically not  
703 as far extended into the pre-midnight sector and is more localized around midnight  
704 (Section 3.4).
- 705 • The spatial morphology of the dawn-cell extension mode (PC3) for STEVE events  
706 is significantly more pronounced and farther extending into the pre-midnight sector  
707 than PC3 for non-STEVE substorm events (Figure 5, Figure 8). There is a direct  
708 relationship observed between the maximum of PC3 coefficients and the extent of the  
709 dawn-cell extension in terms of magnitude and penetration depth into the dusk cell  
710 for both categories of events. Due to the spatial morphology differences in PC3, the  
711 dawn-cell extension observed at the maximum of PC3 coefficients for STEVE events  
712 tends to be more intense than that observed for non-STEVE substorm events (Figure  
713 11).

## 714 **Timing**

- 715 • Although there is variability among individual events, typically during STEVE events  
716 the dawn cell extension starts during the growth phase of substorm, persisting all the  
717 way through the recovery phase of substorm (Section 3.6). Non-STEVE substorm  
718 events also have variations among individual events, but for the majority of events  
719 the dawn cell extension is visually detected during the growth phase through the end  
720 of the expansion phase of substorm (Section 3.6).
- 721 • There are also several notable differences that have been identified related to the  
722 timing in PC coefficients variation over the duration of STEVE and non-STEVE sub-  
723 storm events (Section 4 Table 4). For STEVE events, the median of PC1 coefficients  
724 continues to increase during the substorm recovery phase as opposed to approaching  
725 zero as observed for non-STEVE substorms (Figure 11). This difference in the evo-  
726 lution of PC1 coefficients is related to the prolonged dawn-dusk asymmetry observed  
727 for STEVE events.

## 728 **Relationship to Geomagnetic Activity Parameters**

- 729 • Although further investigation is required to understand physical connections between  
730 IMF and modes of variability of global convection patterns, notable differences have  
731 been observed in IMF By and IMF Bz between STEVE and non-STEVE substorm  
732 events. The dawn-cell extension associated with STEVE events is found largely un-  
733 related to IMF By, which is in agreement with the past studies. While the median  
734 of IMF By is mostly negative for the 3 hour duration of superposed epoch analy-  
735 sis for STEVE events (Figure 6 (e)), for non-STEVE substorms, IMF By is mostly  
736 positive (Figure 9 (e)). The temporal variation of the median of IMF Bz, reaching  
737 to the greatest negative value at substorm onset, is generally similar between these  
738 two category of events, but the variation is more distinct for non-STEVE substorms  
739 (Figures 6 (h) and 9 (h)).
- 740 • The greatest minimum magnitude of the AL-index for STEVE events is -614 nT and  
741 the minimum AL-index for non-STEVE substorm events is found to be -519 nT (2.1.  
742 This result is consistent with the GallardoLacourt et al. (2018) work wherein larger  
743 AL values and a long-lasting expansion phase have been found to be associated with  
744 STEVE events. Although the mean magnitude of AL index is about 100 nT stronger  
745 for the STEVE events analyzed in this study, there is no clear indication that the  
746 strength of AL could be used to predict the likelihood of observing a stronger (or  
747 weaker) dawn-cell extension. As an example of this, the event study reported by

748 Nishimura et al. (2020) and presented as a case study in Section 3.7 shows one of the  
 749 most pronounced dawn-cell westward extension, but it is not among the events with  
 750 greatest AL minimum magnitudes.

751 In summary, the global modes of high-latitude ionospheric electrodynamics associated  
 752 with optical STEVE events characterized in this study provide an important clue to better  
 753 understand what makes STEVE events different from other substorms, and helps to further  
 754 unravel physical mechanisms behind these STEVE events. In addition, this investigation  
 755 showcases the exceptional capabilities of AMGeO software when utilized as a data-mining re-  
 756 search tool for uncovering unknown physical characteristics of high-latitude electrodynamics  
 757 from large amounts of geospace data sets. Our future work with AMGeO includes analyzing  
 758 different features of high-latitude electrodynamics during SAPS and SAID events by using  
 759 previously analyzed events [e.g., Archer et al. (2019a); Erickson et al. (2011)]; such study  
 760 could help us understand the global ionospheric conditions that give rise to the extreme  
 761 SAID parameters detected during STEVE events.

## 762 Acknowledgments

763 We are grateful and would like to show appreciation to Elizabeth MacDonald for her sup-  
 764 port on the STEVE research and help with citizen science data at the initial stage of  
 765 the study. We would also like to extend a special thanks and appreciation to the Boul-  
 766 der Solar Alliance REU program and Martin Snow. VS would like to thank Starr Svaldi  
 767 for supporting her and for her proofreading expertise. This study is mainly supported  
 768 by the National Science Foundation (NSF) ICER 1928403 and AGS 1848544 awards to  
 769 the University of Colorado Boulder. BGL is supported by a NASA Postdoctoral Pro-  
 770 gram (NPP) fellowship at NASA GSFC, administered by Oak Ridge Associated Univer-  
 771 sities (ORAU) under contract with NASA. AMGeO open source software is available from  
 772 <https://amgeo.colorado.edu/> upon registration. AMGeO is supported by the NSF Earth-  
 773 Cube awards ICER 1928403, ICER 1928327, and ICER 1928358. We acknowledge the use  
 774 of SuperDARN data (<http://vt.superdarn.org/tiki-index.php>). SuperDARN is a collection  
 775 of radars funded by national scientific funding agencies of Australia, Canada, China, France,  
 776 Italy, Japan, Norway, South Africa, United Kingdom and the United States of America. We  
 777 acknowledge the use of the substorm timing list identified by the Newell and Gjerloev tech-  
 778 nique (Newell and Gjerloev, 2011), the SMU and SML indices (Newell and Gjerloev, 2011),  
 779 magnetometer data distributed by the SuperMAG collaboration (<https://supermag.jhuapl.edu>),  
 780 Gjerloev et al. 2012). For the ground magnetometer data we acknowledge: INTERMAG-  
 781 NET, Alan Thomson; CARISMA, PI Ian Mann; CANMOS, Geomagnetism Unit of the  
 782 Geological Survey of Canada; The S-RAMP Database, PI K. Yumoto and Dr. K. Shiokawa;  
 783 The SPIDR database; AARI, PI Oleg Troshichev; The MACCS program, PI M. Engebret-  
 784 son; GIMA; MEASURE, UCLA IGPP and Florida Institute of Technology; SAMBA, PI  
 785 Eftyhia Zesta; 210 Chain, PI K. Yumoto; SAMNET, PI Farideh Honary; IMAGE, PI Liisa  
 786 Juusola; Finnish Meteorological Institute, PI Liisa Juusola; Sodankyl Geophysical Observa-  
 787 tory, PI Tero Raita; UiT the Arctic University of Norway, Troms Geophysical Observatory,  
 788 PI Magnar G. Johnsen; GFZ German Research Centre For Geosciences, PI Jrgen Matzka;  
 789 Institute of Geophysics, Polish Academy of Sciences, PI Anne Neska and Jan Reda; Po-  
 790 lar Geophysical Institute, PI Alexander Yahnin and Yarolav Sakharov; Geological Survey  
 791 of Sweden, PI Gerhard Schwarz; Swedish Institute of Space Physics, PI Masatoshi Ya-  
 792 mauchi; AUTUMN, PI Martin Connors; DTU Space, Thom Edwards and PI Anna Willer;  
 793 South Pole and McMurdo Magnetometer, PI's Louis J. Lanzarotti and Alan T. Weatherwax;  
 794 ICESTAR; RAPIDMAG; British Antarctic Survey; McMac, PI Dr. Peter Chi; BGS, PI Dr.  
 795 Susan Macmillan; Pushkov Institute of Terrestrial Magnetism, Ionosphere and Radio Wave  
 796 Propagation (IZMIRAN); MFGI, PI B. Heilig; Institute of Geophysics, Polish Academy of  
 797 Sciences, PI Anne Neska and Jan Reda; University of LAquila, PI M. Vellante; BCMT,  
 798 V. Lesur and A. Chambodut; Data obtained in cooperation with Geoscience Australia, PI  
 799 Andrew Lewis; AALPIP, co-PIs Bob Clauer and Michael Hartinger; SuperMAG, PI Jesper  
 800 W. Gjerloev; Data obtained in cooperation with the Australian Bureau of Meteorology, PI

801 Richard Marshall. The OMNI data were obtained from the GSFC/SPDF OMNIWeb inter-  
 802 face and can be acquired at <https://omniweb.gsfc.nasa.gov> The Redline Emission Geospace  
 803 Observatory (REGO) is a joint Canada Foundation for Innovation and Canadian Space  
 804 Agency project developed by the University of Calgary. THEMIS and REGO ASI data can  
 805 be obtained from <http://data.phys.ucalgary.ca>. The Swarm satellite A and C data is used  
 806 from the level 1b calibrated, validated instrument data made accessible to the public through  
 807 the European Space Agency (<https://swarm-diss.eo.esa.int>). All AMGeO ionospheric con-  
 808 vection patterns used in this study are available at <https://osf.io/26ae5/>.

## 809 References

- 810 AMGeO Collaboration. (2019, December). *A Collaborative Data Science Platform for*  
 811 *the Geospace Community: Assimilative Mapping of Geospace Observations (AMGeO)*  
 812 *v1.0.0* (Tech. Rep.). (Publisher: Zenodo) doi: 10.5281/zenodo.3564914
- 813 Archer, W. E., Gallardo-Lacourt, B., Perry, G. W., St.-Maurice, J. P., Buchert, S. C., &  
 814 Donovan, E. (2019a). Steve: The optical signature of intense subauroral ion drifts.  
 815 *Geophysical Research Letters*, *46*(12), 6279–6286. Retrieved from [https://agupubs](https://agupubs.onlinelibrary.wiley.com/doi/abs/10.1029/2019GL082687)  
 816 [.onlinelibrary.wiley.com/doi/abs/10.1029/2019GL082687](https://agupubs.onlinelibrary.wiley.com/doi/abs/10.1029/2019GL082687) doi: [https://doi](https://doi.org/10.1029/2019GL082687)  
 817 [.org/10.1029/2019GL082687](https://doi.org/10.1029/2019GL082687)
- 818 Archer, W. E., Maurice, J.-P. S. ., GallardoLacourt, B., Perry, G. W., Cully,  
 819 C. M., Donovan, E., ... Eurich, D. (2019b). The Vertical Distribution  
 820 of the Optical Emissions of a Steve and Picket Fence Event. *Geophys-*  
 821 *ical Research Letters*, *46*(19), 10719–10725. Retrieved 2021-03-02, from  
 822 <https://agupubs.onlinelibrary.wiley.com/doi/abs/10.1029/2019GL084473>  
 823 (\_eprint: <https://agupubs.onlinelibrary.wiley.com/doi/pdf/10.1029/2019GL084473>)  
 824 doi: <https://doi.org/10.1029/2019GL084473>
- 825 Chisham, G., Lester, M., Milan, S. E., Freeman, M. P., Bristow, W. A., Grocott, A.,  
 826 ... Walker, A. D. M. (2007, January). A decade of the Super Dual Auroral Radar  
 827 Network (SuperDARN): scientific achievements, new techniques and future directions.  
 828 *Surveys in Geophysics*, *28*(1), 33–109. Retrieved 2021-03-02, from [https://doi.org/](https://doi.org/10.1007/s10712-007-9017-8)  
 829 [10.1007/s10712-007-9017-8](https://doi.org/10.1007/s10712-007-9017-8) doi: 10.1007/s10712-007-9017-8
- 830 Cousins, E. D. P., & Shepherd, S. G. (2010). A dynamical model of high-latitude  
 831 convection derived from SuperDARN plasma drift measurements. *Journal of*  
 832 *Geophysical Research: Space Physics*, *115*(A12). Retrieved 2021-03-04, from  
 833 <https://agupubs.onlinelibrary.wiley.com/doi/abs/10.1029/2010JA016017>  
 834 (\_eprint: <https://agupubs.onlinelibrary.wiley.com/doi/pdf/10.1029/2010JA016017>)  
 835 doi: <https://doi.org/10.1029/2010JA016017>
- 836 Erickson, P. J., Beroz, F., & Miskin, M. Z. (2011). Statistical characterization of the amer-  
 837 ican sector subauroral polarization stream using incoherent scatter radar. *Journal of*  
 838 *Geophysical Research: Space Physics*, *116*(A5). Retrieved from [https://agupubs](https://agupubs.onlinelibrary.wiley.com/doi/abs/10.1029/2010JA015738)  
 839 [.onlinelibrary.wiley.com/doi/abs/10.1029/2010JA015738](https://agupubs.onlinelibrary.wiley.com/doi/abs/10.1029/2010JA015738) doi: [https://doi](https://doi.org/10.1029/2010JA015738)  
 840 [.org/10.1029/2010JA015738](https://doi.org/10.1029/2010JA015738)
- 841 Forsyth, C., Rae, I. J., Coxon, J. C., Freeman, M. P., Jackman, C. M., Gjerloev, J.,  
 842 & Fazakerley, A. N. (2015). A new technique for determining substorm onsets  
 843 and phases from indices of the electrojet (sophie). *Journal of Geophysical Re-*  
 844 *search: Space Physics*, *120*(12), 10,592–10,606. Retrieved from [https://agupubs](https://agupubs.onlinelibrary.wiley.com/doi/abs/10.1002/2015JA021343)  
 845 [.onlinelibrary.wiley.com/doi/abs/10.1002/2015JA021343](https://agupubs.onlinelibrary.wiley.com/doi/abs/10.1002/2015JA021343) doi: [https://doi](https://doi.org/10.1002/2015JA021343)  
 846 [.org/10.1002/2015JA021343](https://doi.org/10.1002/2015JA021343)
- 847 Frey, H. U., Mende, S. B., Angelopoulos, V., & Donovan, E. F. (2004). Substorm on-  
 848 set observations by image-fuv. *Journal of Geophysical Research: Space Physics*,  
 849 *109*(A10). Retrieved from [https://agupubs.onlinelibrary.wiley.com/doi/abs/](https://agupubs.onlinelibrary.wiley.com/doi/abs/10.1029/2004JA010607)  
 850 [10.1029/2004JA010607](https://agupubs.onlinelibrary.wiley.com/doi/abs/10.1029/2004JA010607) doi: <https://doi.org/10.1029/2004JA010607>
- 851 Gallardo-Lacourt, B., Perry, G. W., Archer, W. E., & Donovan, E. (2019). *How*  
 852 *Did We Miss This? An Upper Atmospheric Discovery Named STEVE* (No. 100).  
 853 Retrieved 2021-03-17, from <https://eos.org/features/how-did-we-miss-this-an>

- 854 -upper-atmospheric-discovery-named-steve doi: <https://doi.org/10.1029/2019EO117351>  
855
- 856 GallardoLacourt, B., Nishimura, Y., Donovan, E., Gillies, D. M., Perry, G. W., Archer,  
857 W. E., ... Spanswick, E. L. (2018). A Statistical Analysis of STEVE. *Journal of Geo-*  
858 *physical Research: Space Physics*, 123(11), 9893–9905. Retrieved 2021-02-28, from  
859 <https://agupubs.onlinelibrary.wiley.com/doi/abs/10.1029/2018JA025368>  
860 (eprint: <https://agupubs.onlinelibrary.wiley.com/doi/pdf/10.1029/2018JA025368>)  
861 doi: <https://doi.org/10.1029/2018JA025368>
- 862 Gillies, D. M., Donovan, E., Hampton, D., Liang, J., Connors, M., Nishimura, Y.,  
863 ... Spanswick, E. (2019). First Observations From the TREx Spectrograph:  
864 The Optical Spectrum of STEVE and the Picket Fence Phenomena. *Geo-*  
865 *physical Research Letters*, 46(13), 7207–7213. Retrieved 2021-03-12, from  
866 <https://agupubs.onlinelibrary.wiley.com/doi/abs/10.1029/2019GL083272>  
867 (eprint: <https://agupubs.onlinelibrary.wiley.com/doi/pdf/10.1029/2019GL083272>)  
868 doi: <https://doi.org/10.1029/2019GL083272>
- 869 Gjerloev, J. W. (2012). The SuperMAG data processing technique. *Journal of*  
870 *Geophysical Research: Space Physics*, 117(A9). Retrieved 2021-03-04, from  
871 <https://agupubs.onlinelibrary.wiley.com/doi/abs/10.1029/2012JA017683>  
872 (eprint: <https://agupubs.onlinelibrary.wiley.com/doi/pdf/10.1029/2012JA017683>)  
873 doi: <https://doi.org/10.1029/2012JA017683>
- 874 Gkioulidou, M., Wang, C.-P., Lyons, L. R., & Wolf, R. A. (2009). Formation of  
875 the harang reversal and its dependence on plasma sheet conditions: Rice con-  
876 vection model simulations. *Journal of Geophysical Research: Space Physics*,  
877 114(A7). Retrieved from [https://agupubs.onlinelibrary.wiley.com/doi/abs/](https://agupubs.onlinelibrary.wiley.com/doi/abs/10.1029/2008JA013955)  
878 [10.1029/2008JA013955](https://doi.org/10.1029/2008JA013955) doi: <https://doi.org/10.1029/2008JA013955>
- 879 Grocott, A., Milan, S. E., Yeoman, T. K., Sato, N., Yukimatu, A. S., &  
880 Wild, J. A. (2010). Superposed epoch analysis of the ionospheric convec-  
881 tion evolution during substorms: IMF BY dependence. *Journal of Geo-*  
882 *physical Research: Space Physics*, 115(A5). Retrieved 2021-03-11, from  
883 <https://agupubs.onlinelibrary.wiley.com/doi/abs/10.1029/2010JA015728>  
884 (eprint: <https://agupubs.onlinelibrary.wiley.com/doi/pdf/10.1029/2010JA015728>)  
885 doi: <https://doi.org/10.1029/2010JA015728>
- 886 Harang, L. (1946). The mean field of disturbance of polar geomagnetic storms. *Terrestrial*  
887 *Magnetism and Atmospheric Electricity*, 51(3), 353-380. Retrieved from [https://](https://agupubs.onlinelibrary.wiley.com/doi/abs/10.1029/TE051i003p00353)  
888 [agupubs.onlinelibrary.wiley.com/doi/abs/10.1029/TE051i003p00353](https://doi.org/10.1029/TE051i003p00353) doi:  
889 <https://doi.org/10.1029/TE051i003p00353>
- 890 Harding, B. J., Mende, S. B., Triplett, C. C., & Wu, Y.-J. J. (2020). A  
891 Mechanism for the STEVE Continuum Emission. *Geophysical Research*  
892 *Letters*, 47(7), e2020GL087102. Retrieved 2021-03-12, from [https://](https://agupubs.onlinelibrary.wiley.com/doi/abs/10.1029/2020GL087102)  
893 [agupubs.onlinelibrary.wiley.com/doi/abs/10.1029/2020GL087102](https://doi.org/10.1029/2020GL087102) (eprint:  
894 <https://agupubs.onlinelibrary.wiley.com/doi/pdf/10.1029/2020GL087102>) doi:  
895 <https://doi.org/10.1029/2020GL087102>
- 896 Kamide, Y., & Kokubun, S. (1996). Two-component auroral electrojet: Importance  
897 for substorm studies. *Journal of Geophysical Research: Space Physics*, 101(A6),  
898 13027-13046. Retrieved from [https://agupubs.onlinelibrary.wiley.com/doi/](https://agupubs.onlinelibrary.wiley.com/doi/abs/10.1029/96JA00142)  
899 [abs/10.1029/96JA00142](https://doi.org/10.1029/96JA00142) doi: <https://doi.org/10.1029/96JA00142>
- 900 Kivelson, M. G., & Russell, C. T. (1995). *Introduction to space physics*. Cambridge  
901 University Press. doi: <https://doi.org/10.1017/9781139878296>
- 902 Liang, J., Shen, Y., Knudsen, D., Spanswick, E., Burchill, J., & Donovan, E. (2019).  
903 e-POP and Red Line Optical Observations of Alfvnic Auroras. *Journal of Geo-*  
904 *physical Research: Space Physics*, 124(6), 4672–4696. Retrieved 2021-03-12, from  
905 <https://agupubs.onlinelibrary.wiley.com/doi/abs/10.1029/2019JA026679>  
906 (eprint: <https://agupubs.onlinelibrary.wiley.com/doi/pdf/10.1029/2019JA026679>)  
907 doi: <https://doi.org/10.1029/2019JA026679>
- 908 MacDonald, E. A., Donovan, E., Nishimura, Y., Case, N. A., Gillies, D. M., Gallardo-

- 909 Lacourt, B., ... Schofield, I. (2018, March). New science in plain sight: Citizen sci-  
 910 entists lead to the discovery of optical structure in the upper atmosphere. *Science Ad-  
 911 vances*, 4(3), eaaq0030. Retrieved 2021-03-04, from [https://advances.sciencemag](https://advances.sciencemag.org/content/4/3/eaaq0030)  
 912 [.org/content/4/3/eaaq0030](https://advances.sciencemag.org/content/4/3/eaaq0030) (Publisher: American Association for the Advance-  
 913 ment of Science Section: Research Article) doi: 10.1126/sciadv.aaq0030
- 914 Matsuo, T. (2020). Recent Progress on Inverse and Data Assimilation Procedure for  
 915 High-Latitude Ionospheric Electrodynamics. In M. W. Dunlop & H. Lhr (Eds.),  
 916 *Ionospheric Multi-Spacecraft Analysis Tools: Approaches for Deriving Ionospheric  
 917 Parameters* (pp. 219–232). Cham: Springer International Publishing. Retrieved  
 918 2021-03-02, from [https://doi.org/10.1007/978-3-030-26732-2\\_10](https://doi.org/10.1007/978-3-030-26732-2_10) doi: 10.1007/  
 919 978-3-030-26732-2\_10
- 920 McGranaghan, R., Knipp, D. J., Matsuo, T., & Cousins, E. (2016). Optimal inter-  
 921 polation analysis of high-latitude ionospheric Hall and Pedersen conductivities:  
 922 Application to assimilative ionospheric electrodynamics reconstruction. *Journal of  
 923 Geophysical Research: Space Physics*, 121(5), 4898–4923. Retrieved 2021-03-02, from  
 924 <https://agupubs.onlinelibrary.wiley.com/doi/abs/10.1002/2016JA022486>  
 925 (eprint: <https://agupubs.onlinelibrary.wiley.com/doi/pdf/10.1002/2016JA022486>)  
 926 doi: <https://doi.org/10.1002/2016JA022486>
- 927 McGranaghan, R., Knipp, D. J., Matsuo, T., Godinez, H., Redmon, R. J., Solomon, S. C.,  
 928 & Morley, S. K. (2015, December). Modes of high-latitude auroral conductance  
 929 variability derived from DMSP energetic electron precipitation observations: Empir-  
 930 ical orthogonal function analysis: PRIMARY MODES OF CONDUCTANCE VARI-  
 931 ABILITY. *Journal of Geophysical Research: Space Physics*, 120(12), 11,013–11,031.  
 932 Retrieved 2021-03-02, from <http://doi.wiley.com/10.1002/2015JA021828> doi:  
 933 10.1002/2015JA021828
- 934 Newell, P. T., & Gjerloev, J. W. (2011). Evaluation of SuperMAG auroral elec-  
 935 trojet indices as indicators of substorms and auroral power. *Journal of Geo-  
 936 physical Research: Space Physics*, 116(A12). Retrieved 2021-03-02, from  
 937 <https://agupubs.onlinelibrary.wiley.com/doi/abs/10.1029/2011JA016779>  
 938 (eprint: <https://agupubs.onlinelibrary.wiley.com/doi/pdf/10.1029/2011JA016779>)  
 939 doi: <https://doi.org/10.1029/2011JA016779>
- 940 Newell, P. T., Sotirelis, T., & Wing, S. (2009). Diffuse, monoenergetic, and  
 941 broadband aurora: The global precipitation budget. *Journal of Geo-  
 942 physical Research: Space Physics*, 114(A9). Retrieved 2021-03-11, from  
 943 <https://agupubs.onlinelibrary.wiley.com/doi/abs/10.1029/2009JA014326>  
 944 (eprint: <https://agupubs.onlinelibrary.wiley.com/doi/pdf/10.1029/2009JA014326>)  
 945 doi: <https://doi.org/10.1029/2009JA014326>
- 946 Nishimura, Y., GallardoLacourt, B., Zou, Y., Mishin, E., Knudsen, D. J., Donovan,  
 947 E. F., ... Raybell, R. (2019). Magnetospheric Signatures of STEVE: Impli-  
 948 cations for the Magnetospheric Energy Source and Interhemispheric Conjugacy.  
 949 *Geophysical Research Letters*, 46(11), 5637–5644. Retrieved 2021-03-11, from  
 950 <https://agupubs.onlinelibrary.wiley.com/doi/abs/10.1029/2019GL082460>  
 951 (eprint: <https://agupubs.onlinelibrary.wiley.com/doi/pdf/10.1029/2019GL082460>)  
 952 doi: <https://doi.org/10.1029/2019GL082460>
- 953 Nishimura, Y., Lyons, L., Zou, S., Angelopoulos, V., & Mende, S. (2010). Substorm  
 954 triggering by new plasma intrusion: Themis all-sky imager observations. *Journal of  
 955 Geophysical Research: Space Physics*, 115(A7). Retrieved from [https://agupubs](https://agupubs.onlinelibrary.wiley.com/doi/abs/10.1029/2009JA015166)  
 956 [.onlinelibrary.wiley.com/doi/abs/10.1029/2009JA015166](https://agupubs.onlinelibrary.wiley.com/doi/abs/10.1029/2009JA015166) doi: [https://doi](https://doi.org/10.1029/2009JA015166)  
 957 [.org/10.1029/2009JA015166](https://doi.org/10.1029/2009JA015166)
- 958 Nishimura, Y., Yang, J., Weygand, J. M., Wang, W., Kosar, B., Donovan, E. F., ...  
 959 Nishitani, N. (2020). Magnetospheric Conditions for STEVE and SAID: Particle  
 960 Injection, Substorm Surge, and Field-Aligned Currents. *Journal of Geophysical  
 961 Research: Space Physics*, 125(8), e2020JA027782. Retrieved 2021-02-28, from  
 962 <https://agupubs.onlinelibrary.wiley.com/doi/abs/10.1029/2020JA027782>  
 963 (eprint: <https://agupubs.onlinelibrary.wiley.com/doi/pdf/10.1029/2020JA027782>)

- 964 doi: <https://doi.org/10.1029/2020JA027782>
- 965 Ohtani, S., Gkioulidou, M., Wang, C.-P., & Wolf, R. A. (2016). The harang re-  
966 versal and the interchange stability of the magnetotail. *Journal of Geophysical*  
967 *Research: Space Physics*, *121*(4), 3278-3292. Retrieved from [https://agupubs](https://agupubs.onlinelibrary.wiley.com/doi/abs/10.1002/2015JA022025)  
968 [.onlinelibrary.wiley.com/doi/abs/10.1002/2015JA022025](https://agupubs.onlinelibrary.wiley.com/doi/abs/10.1002/2015JA022025) doi: [https://doi](https://doi.org/10.1002/2015JA022025)  
969 [.org/10.1002/2015JA022025](https://doi.org/10.1002/2015JA022025)
- 970 Redmon, R. J., Denig, W. F., Kilcommons, L. M., & Knipp, D. J. (2017). New  
971 DMSP database of precipitating auroral electrons and ions. *Journal of Geophys-*  
972 *ical Research: Space Physics*, *122*(8), 9056–9067. Retrieved 2021-03-04, from  
973 <https://agupubs.onlinelibrary.wiley.com/doi/abs/10.1002/2016JA023339>  
974 (\_eprint: <https://agupubs.onlinelibrary.wiley.com/doi/pdf/10.1002/2016JA023339>)  
975 doi: <https://doi.org/10.1002/2016JA023339>
- 976 Zou, S., Lyons, L. R., Nicolls, M. J., Heinselman, C. J., & Mende, S. B. (2009).  
977 Nightside ionospheric electrodynamics associated with substorms: Pfiir and themis  
978 asi observations. *Journal of Geophysical Research: Space Physics*, *114*(A12).  
979 Retrieved from [https://agupubs.onlinelibrary.wiley.com/doi/abs/10.1029/](https://agupubs.onlinelibrary.wiley.com/doi/abs/10.1029/2009JA014259)  
980 [2009JA014259](https://agupubs.onlinelibrary.wiley.com/doi/abs/10.1029/2009JA014259) doi: <https://doi.org/10.1029/2009JA014259>

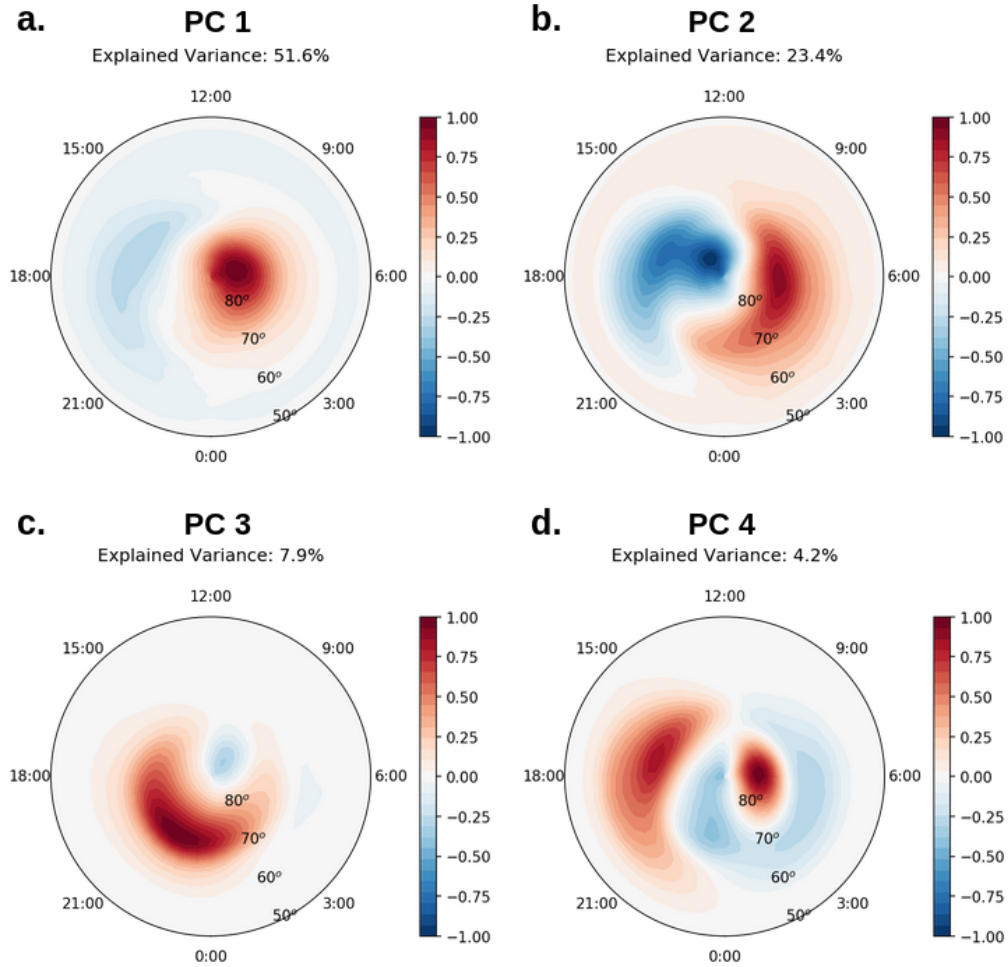


**Figure 5.** Maps for the first four principal components (PC) of electrostatic potential for 32 STEVE events. The total variance explained by each PC is displayed at the top of each map.

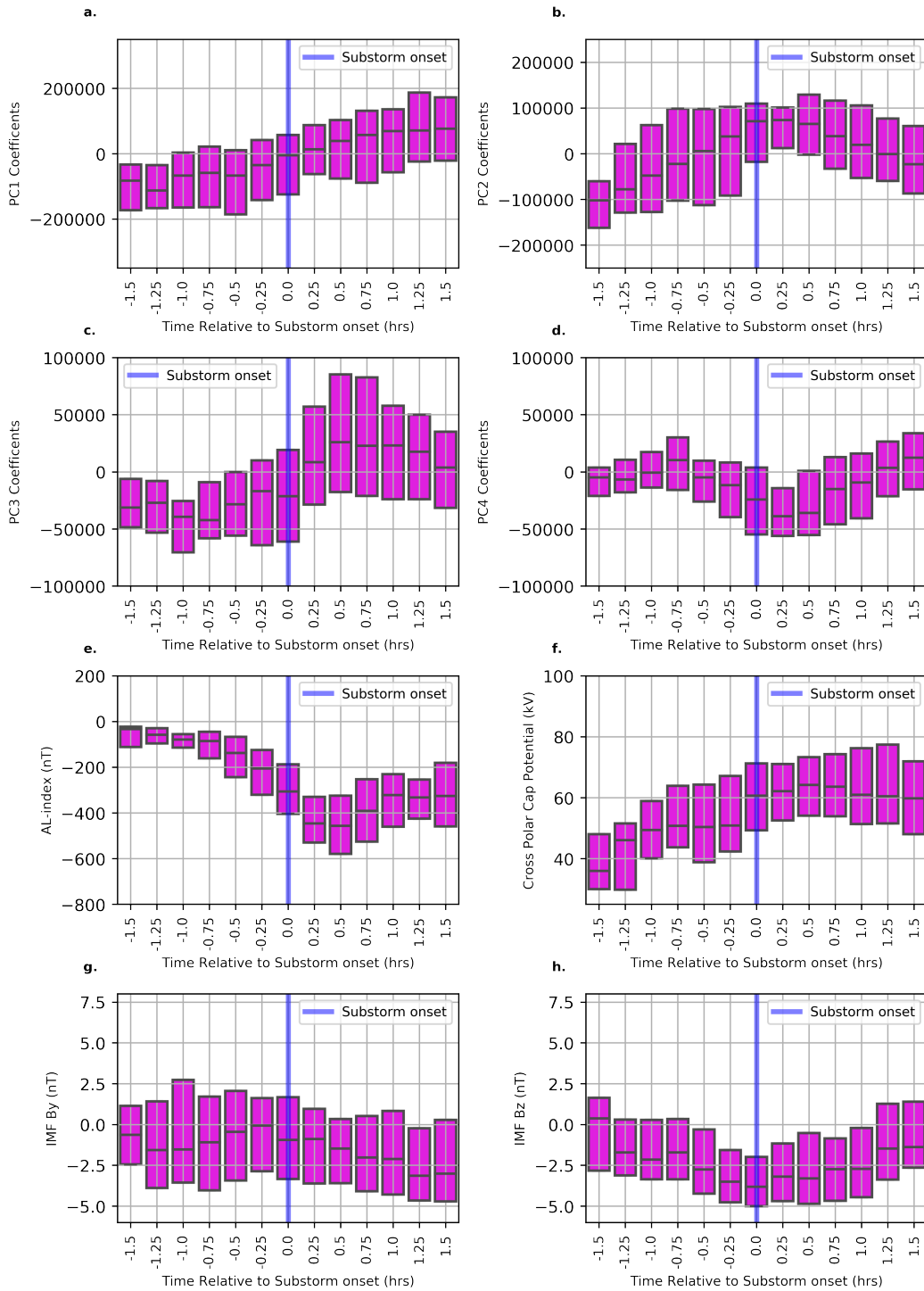


**Figure 6.** Superposed epoch analysis of PC coefficients for STEVE events displayed over a 3-hour duration centered at substorm onset (1.5 hour prior and 1.5 hour post substorm onset time) for the first four modes (a-d). Superposed epoch analysis for AL-index (e), cross-polar cap potential (f), and IMF By and IMF Bz (g-h) shown in the same manner as for PC coefficients.



**Figure 7.** Correlation matrix of PC coefficients, AL-index, AU-index, IMF By, IMF Bz, and cross-polar cap potential for 32 STEVE events.

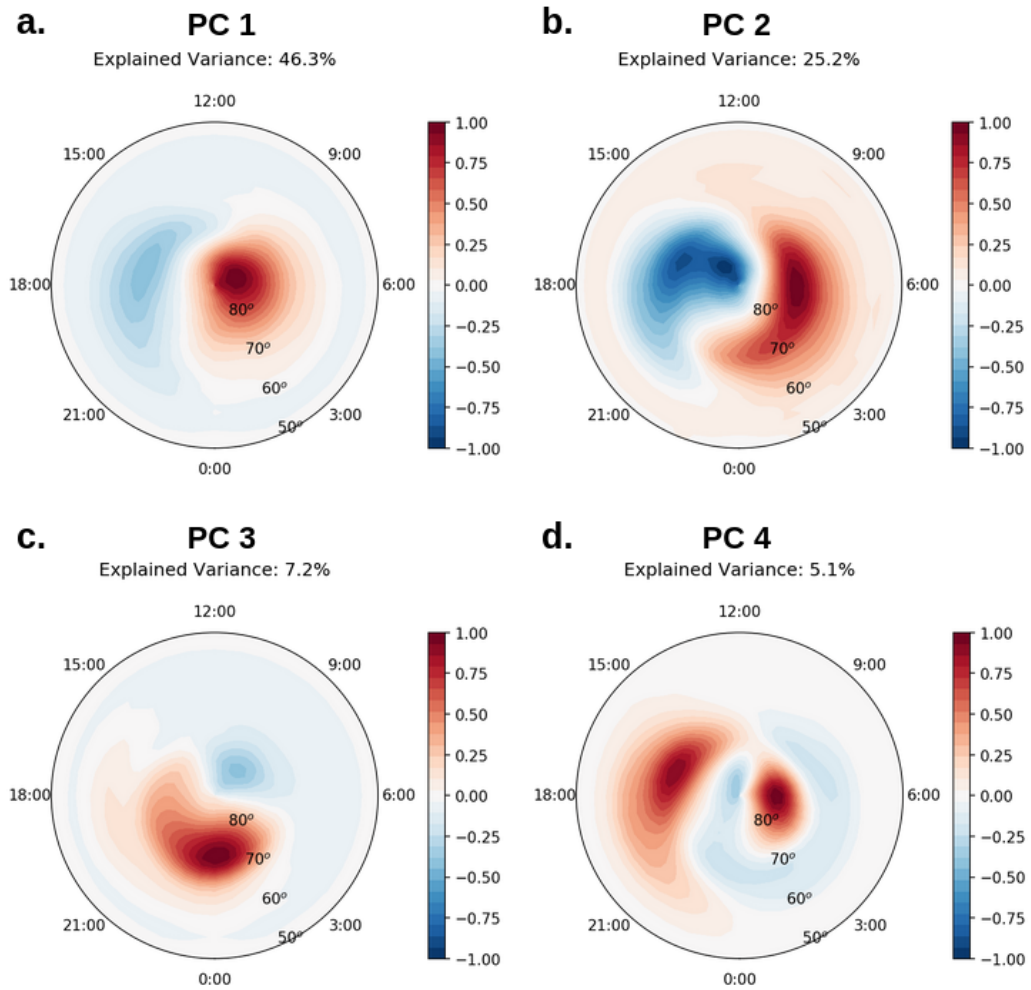


**Figure 8.** (a.)-(d.) PC maps for the first four principal components of electrostatic potential from 32 non-STEVE substorm events. The explained variance ratio is displayed at the top of each PC plot.

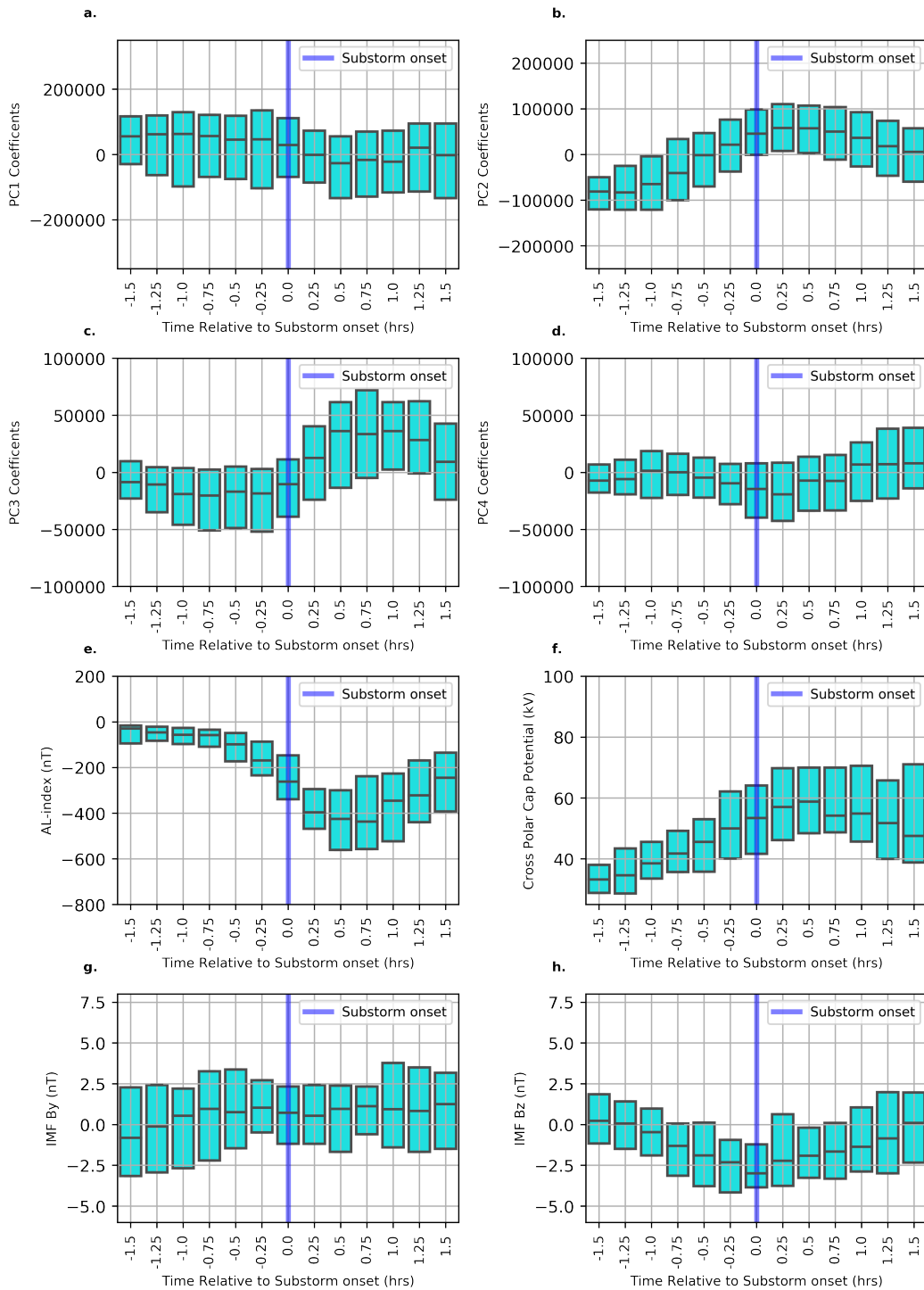


**Figure 9.** Superposed epoch analysis for non-STEVE substorm events is shown, over a 3-hour duration centered at substorm onset (1.5 hour prior and 1.5 hour post substorm onset time), for PC1-PC4 coefficients (a-d), AL-index (e), cross-polar cap potential (f), and IMF By and Bz (g-h).

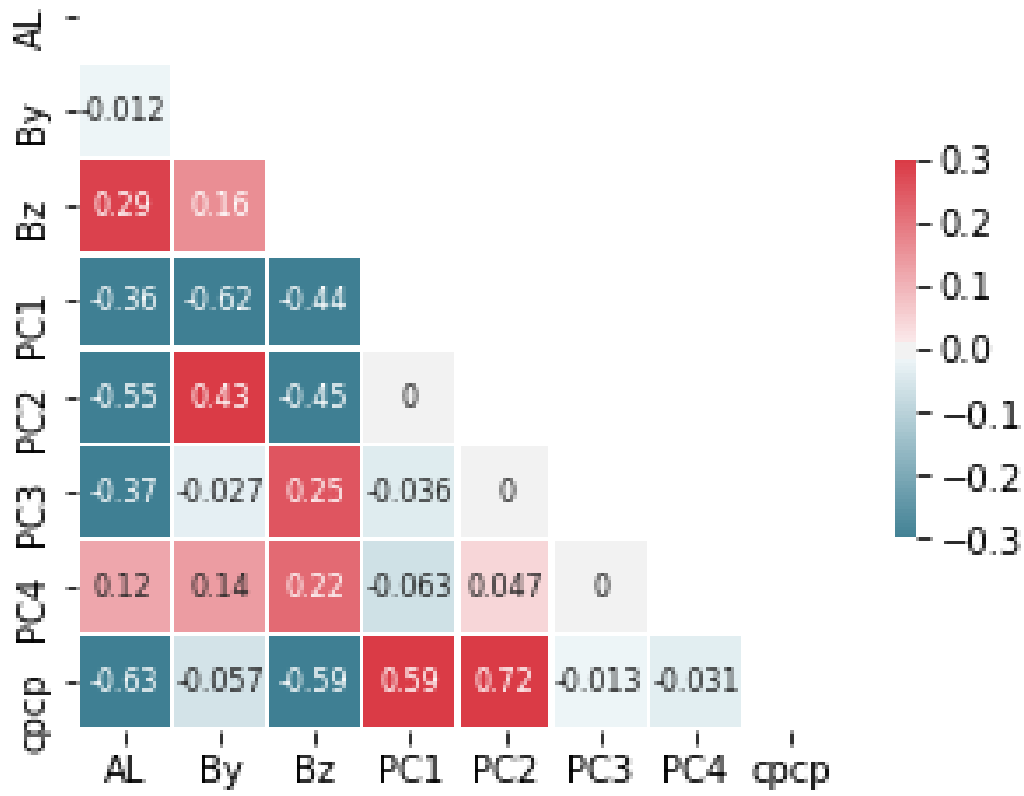


**Figure 10.** Correlation matrix of PC coefficients, AL-index, AU-index, IMF By and Bz, and cross-polar cap potential for 32 non-STEVE substorm events.

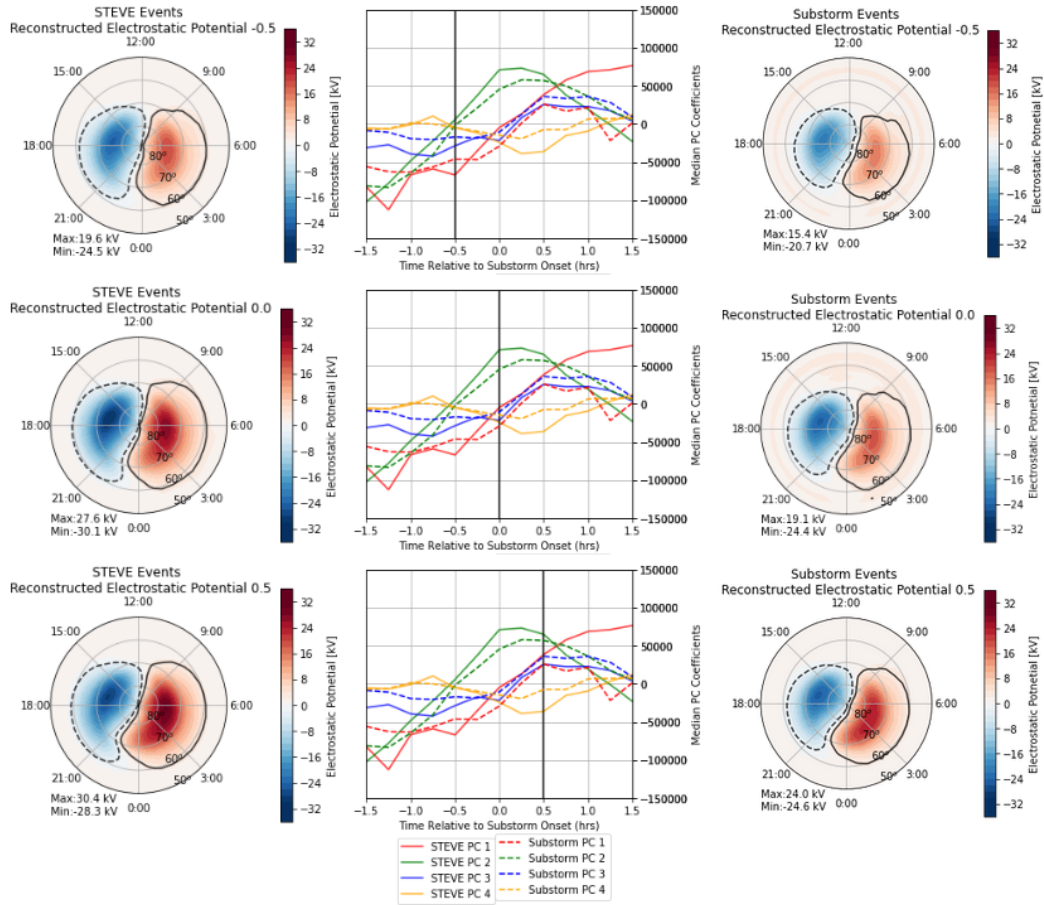


**Figure 11.** Reconstructed electrostatic potential maps derived for 32 STEVE event (left) and 32 non-STEVE substorm events (right) and time series of median PC coefficients (center). Maps at 0.5 hour prior to substorm onset indicated by a black vertical line in the center plot of median PC coefficients time series (top). Maps at substorm onset (middle) and maps 0.5 hour post substorm onset (bottom) shown in the same format as the maps shown on the top.

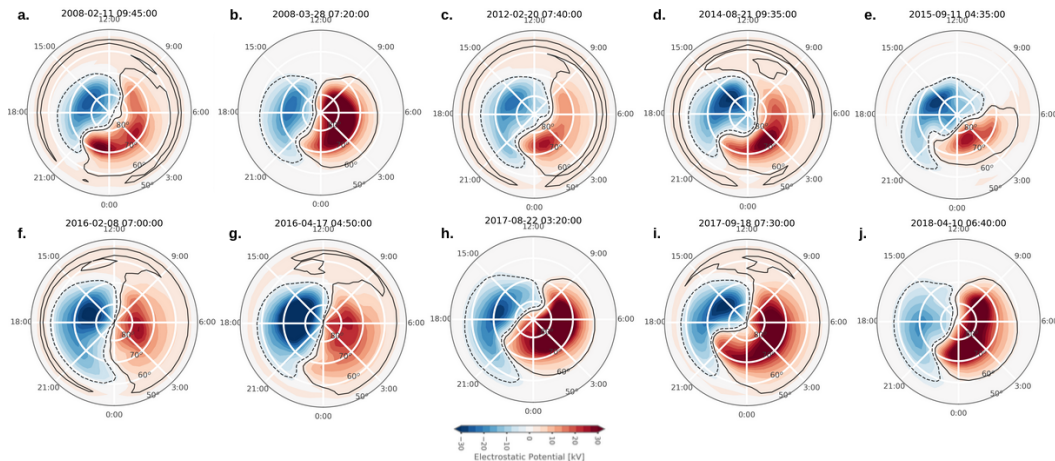


**Figure 12.** AMGeO electrostatic potential maps displayed at the maximum time of dawn-cell extension mode (PC3) for 10 STEVE events that are selected based on SML minimum values.

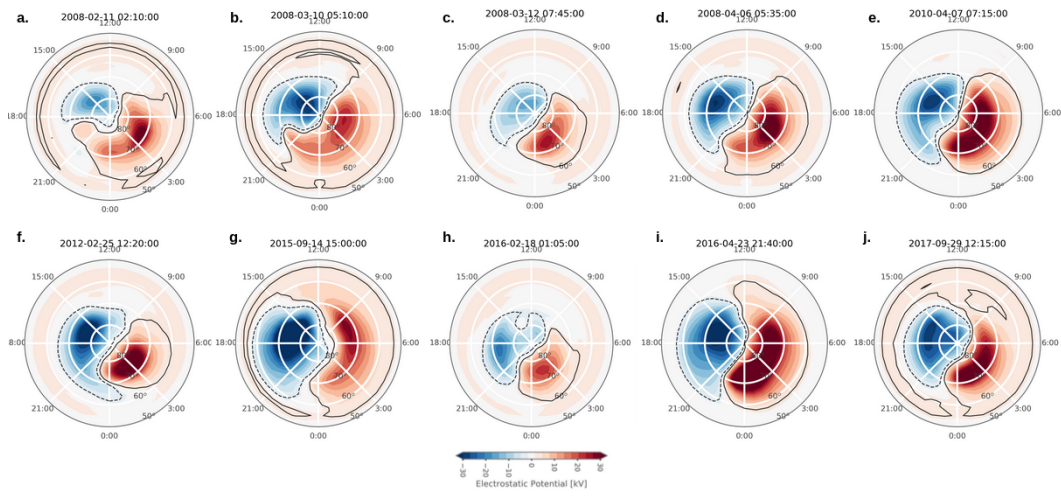


**Figure 13.** AMGeO electrostatic potential maps displayed at the maximum time of dawn-cell extension mode (PC3) for 10 non-STEVE substorm events that are selected based on SML minimum values.

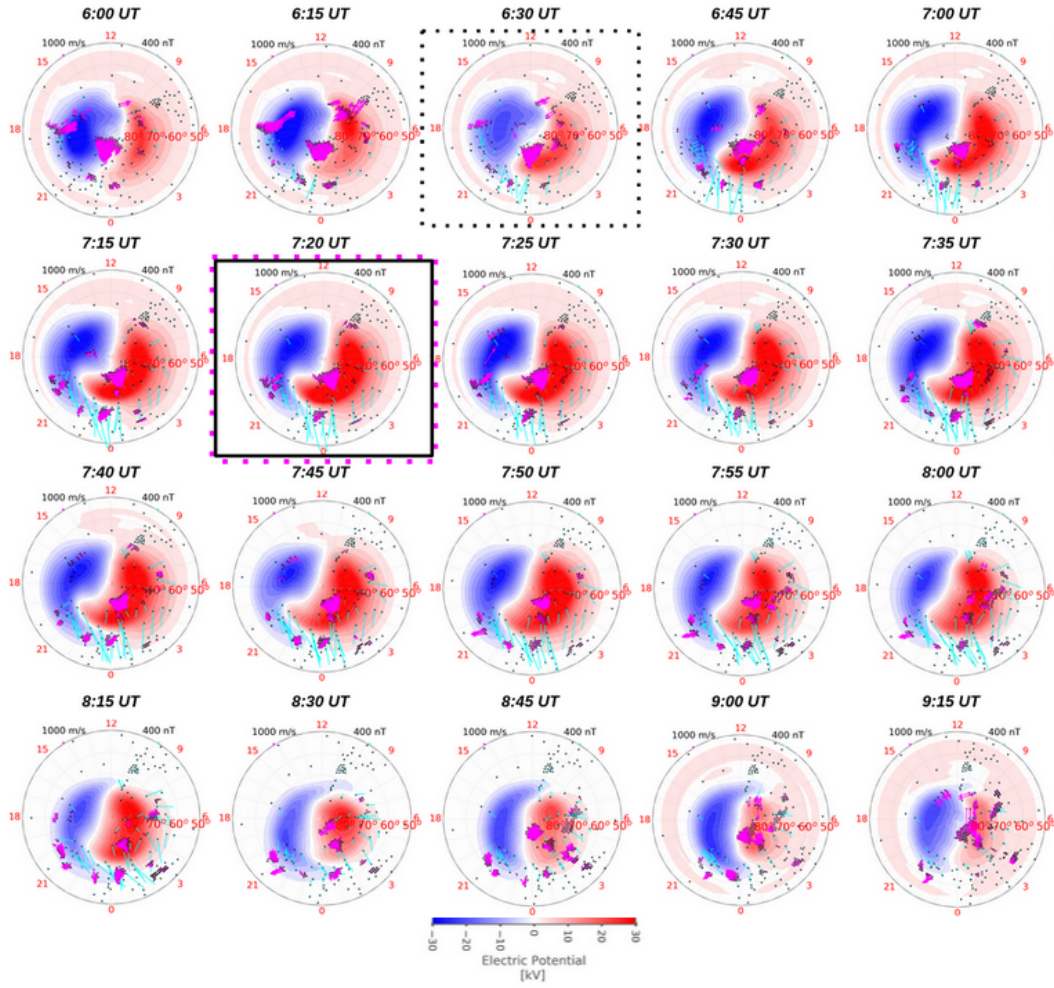


**Figure 14.** AMGeO electrostatic potential maps for the STEVE event on March 26th 2008 displayed from 6:00 to 9:15 UT. The substorm onset for this STEVE event occurs at 6:00 UT as marked with a black dotted box. The SML minimum is -826 nT at 7:20 UT, which is denoted with a solid black box. The STEVE optical onset occurs at the end of the substorm expansion phase at 7:20 UT as marked by a pink dotted box. SuperDARN plasma drift data (magenta) and SuperMAG ground-level magnetic field data (light blue) are superimposed.

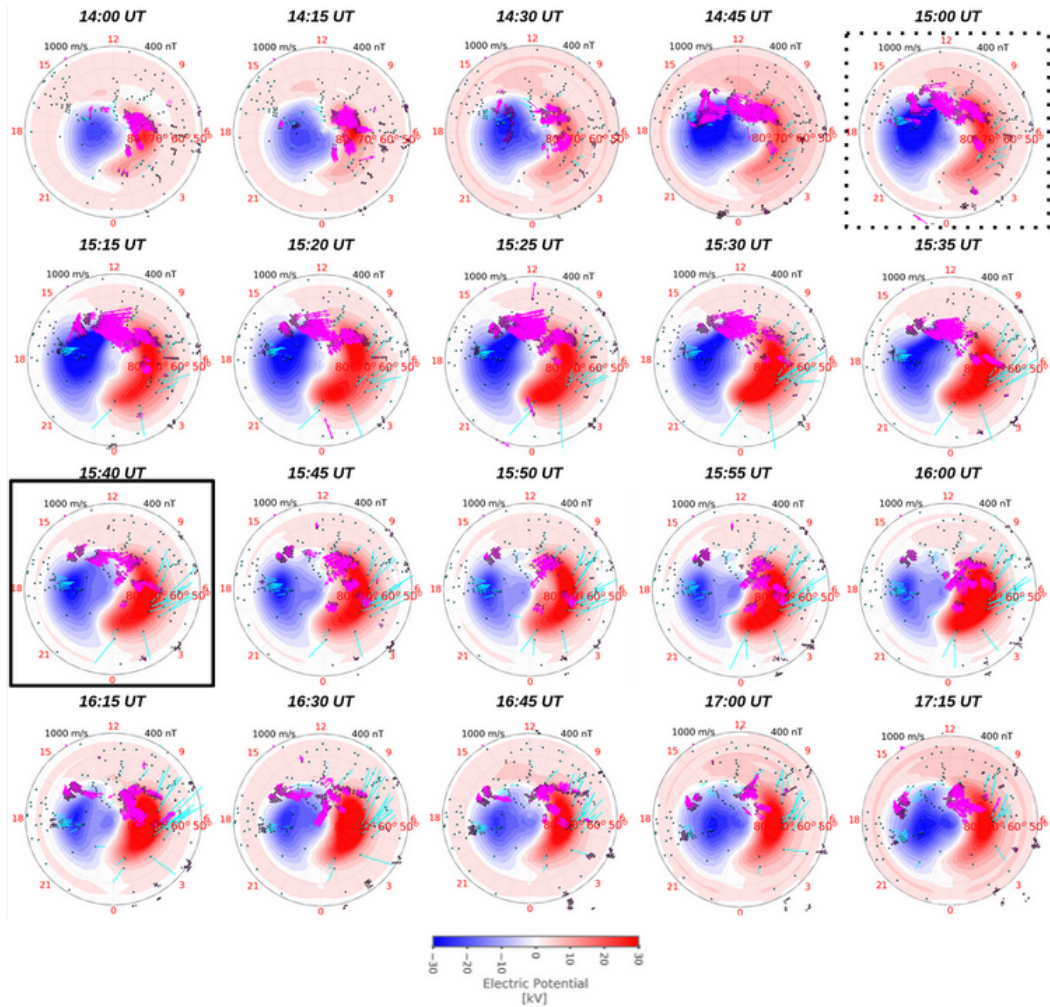


**Figure 15.** AMGeo electrostatic potential maps for non-STEVE substorm event on September 14, 2015 displayed from 14:00 UT to 17:15 UT. The substorm onset is at 15:00 UT as marked with a black dotted box. The SML minimum is -935 nT at 15:40 UT as denoted by a black solid box. SuperDARN plasma drifts (magenta) and SuperMAG ground-level magnetic field observations (light blue) are superimposed.

**Table 4.** Summary of the key differences observed in the PCA results for STEVE and non-STEVE substorm events

<b>PC Coefficients and Convection Pattern Behaviors</b>	
<b>STEVE events</b>	<b>Non-STEVE substorm events</b>
<b><i>PC1 – Dawn-cell intensification mode</i></b>	
PC1 coefficients do not approach zero for 7/10 events after substorm onset, contributing to prolonged dawn-dusk asymmetry (Section 3.6). The median of PC1 coefficients from 32 events does not approach zero after substorm onset and continues to grow for about 1.25 hours (Section 3.5: Figure 11).	PC1 coefficients tends to approach or reach zero at end of recovery phase for 7/10 events, resulting in the return to a symmetrical two-cell convection pattern (Section 3.6). The median of PC1 coefficients from 32 events approach zero after 1.5 hours post substorm onset (Section 3.5: Figure 11).
PC1 behaviors are related to significant dawn cell extension seen in AMGeO electrostatic potential maps lasting over 1.5 hours post substorm onset in 9/10 events (Section 3.6).	PC1 behaviors are related to some dawn cell extension seen in AMGeO electrostatic potential maps lasting over 1.5 hours post substorm onset in 3/10 events (Section 3.6).
<b><i>PC2 – Localized nightside dawn-cell penetrating mode</i></b>	
The peak time of PC2 coefficients vary among 10 individual events, occurring during the expansion phase for 6/10 events and in the recovery phase for 4/10 events (Section 3.6).	The peak time of PC2 coefficients vary considerably among 10 individual events, occurring in the growth phase for 3/10 events, in the expansion phase for 4/10 events, and in the recovery phase for 3/10 events (Section 3.6).
At the peak of PC2, AMGeO electrostatic potential maps show strong dawn-dusk asymmetry on nightside in 10/10 events (Section 3.6).	At the peak of PC2, AMGeO electrostatic potential maps show some dawn-dusk asymmetry on nightside in 10/10 events (Section 3.6).
<b><i>PC3 – Dawn-cell extension mode</i></b>	
The dawn-cell extension morphological feature in PC3 is pronounced and extends into the pre-midnight sector (Section 3.3: Figure 5(c)).	The dawn-cell extension morphological feature in PC3 extends less into the pre-midnight sector and is less pronounced (Section 3.4: Figure 8(c)).
PC3 coefficients start to increase prior to substorm onset (Section 3.5: Figure 11, Section 3.6).	PC3 coefficients start to increase after substorm onset (Section 3.5: Figure 11, Section 3.6).
The peak time of PC3 coefficients occurs during the recovery phase for 7/10 events and in the expansion phase for 3/10 events (Section 3.6).	The peak time of PC3 coefficients occurs in the expansion phase for 6/10 events and in the recovery phase for 4/10 events (Section 3.6).
PC3 behaviours are directly related to peaking of dawn-cell extension seen in AMGeO electrostatic potential maps (Section 3.5: Figure 11, Section 3.6, Section 3.7: Figure 14). AMGeO electrostatic potential maps at the time of PC3 peak show strong dawn-cell extension into the pre-midnight sector in 9/10 events (Section 3.6: Figure 12).	PC3 coefficient behaviours are similar to those observed during STEVE events (Section 3.5: Figure 11). Due to the difference in PC3 morphology itself the AMGeO electrostatic potential maps at the time of PC3 peak shows a less pronounced and more diverse appearance of the dawn-cell extension in 10/10 events (Section 3.6: Figure 13).
<b><i>PC4 – Weak asymmetry mode</i></b>	
PC4 does not contribute to the key differences due to its small magnitudes.	

**Table 5.** Summary of the key differences observed in the cross-polar cap potential for STEVE and non-STEVE substorm events

<b>Cross-Polar Cap Potential</b>	
<b>STEVE events</b>	<b>Non-STEVE substorm events</b>
The mean electrostatic potential estimated from all 32 STEVE events is 48.15 kV (Section 3.2: Figure 4 (a)).	The mean electrostatic potential estimated from all 32 non-STEVE substorm events is 39.32 kV (Section 3.2: Figure 4 (b)).
Larger magnitude of cross-polar cap potential across the 3-hour duration of superposed epoch analysis (Section 3.3: Figure 6 (f)).	Weaker magnitude of cross-polar cap potential across the 3-hour duration of superposed epoch analysis (Section 3.4: Figure 9 (f)).

**Table 6.** Summary of the key differences in IMF By and IMF Bz trends observed during STEVE and non-STEVE substorm events

<b>IMF By and IMF Bz</b>	
<b>STEVE events</b>	<b>Non-STEVE substorm events</b>
IMF By has generally low magnitudes for 32 events, and the median value is predominantly negative across the 3-hour duration of superposed epoch analysis (Section 3.3: Figure 6 (g)).	IMF By has generally low magnitudes for 32 events, and the median value is predominantly positive across the 3-hour duration of superposed epoch analysis (Section 3.4: Figure 9 (g)).
The median of IMF Bz gradually decreases from almost zero at 1.5 hours prior to onset to about -3 nT at substorm onset and gradually grows back to -1.5 nT after 1.5 hours post onset (Section 3.3: Figure 6 (h)). Bz temporal variation is less defined.	The median of IMF Bz decreases from almost zero at 1.5 hours prior to onset to about -3 nT at substorm onset at the slow rate at the beginning and more sharply close to onset. It grows back to nearly zero after 1.5 hours post onset. Bz temporal variation is more defined. (Section 3.4: Figure 9 (h)).